Electronic Supplementary Information

Mononuclear Lanthanide(III)-Oxamate Complexes as New Photoluminescent Field-Induced Single-Molecule Magnets: Solid-State Photophysical and Magnetic Properties

Raphael C.A. Vaz,[a] Isabela O. Esteves,[a] Willian X.C. Oliveira,[a] João Honorato,[b] Felipe T. Martins,[b] Lippy F. Marques,[c] Guilherme L. dos Santos,[c] Ricardo O. Freire,[d] Larissa T. Jesus,[d] Emerson F. Pedroso,[e,f] Wallace C. Nunes,[g] Miguel Julve,[h] and Cynthia L.M. Pereira[a,f*]

[a]Departamento de Química, Instituto de Ciências Exatas, Universidade Federal de Minas Gerais. Av. Antônio Carlos 6627, Pampulha, Belo Horizonte, Minas Gerais, 31270-901 Brazil. e-mail: cynthialopes@ufmg.br

[b]Instituto de Química, Universidade Federal de Goiás, Campus Samambaia Setor Itatiaia, Caixa Postal 131, Goiânia, Goiás, 74001970, Brazil;

[c]Grupo de Materiais Inorgânicos Multifuncionais (GMIM), Universidade do Estado do Rio de Janeiro, Centro de Tecnologia de Ciências, Instituto de Química, Maracanã, Rio de Janeiro, 20550-900, Brazil;

[d]Pople Computational Chemistry Laboratory, Departamento de Química, Universidade Federal de Sergipe, São Cristóvão-SE, 49100-000, Brazil;

[e]Laboratório de Tecnologias Integradas (Intechlab), Centro Federal de Educação Tecnológica de Minas Gerais, Av. Amazonas 5523, Belo Horizonte, Minas Gerais 30421-169, Brazil;

[f]Department of Chemistry, University of California, Berkeley, CA 94720, USA;

[g]Instituto de Física, Universidade Federal Fluminense, Av. Gal. Milton Tavares de Souza, s/nº, Campus da Praia Vermelha, Niterói, Rio de Janeiro, 24210-346, Brazil;

[h]Departament de Química Inorgànica/Instituto de Ciencia Molecular (ICMol), Universitat de València, C/ Catedrático José Beltrán 2, 46980 Paterna (València) Spain.

Corresponding author: cynthialopes@ufmg.br (C.L.M.Pereira)

Keywords: synthesis, crystal structures, magnetic properties, photoluminescence, single-molecule magnets, lanthanides

Experimental

Materials and Methods

All chemicals in this work are analytical grade reagents and they were used as purchasedwithout any further purification. The ethyl *N*-(4-fluorophenyl)oxamate and Ethyl *N*-(4-chlorophenyl)oxamate proligands weresynthesized according to previously described methods.[1,2] The monodeprotonated forms of the halosubstituted oxamic acids [H_2L = *N*-(4-Xphenyl)oxamic acid with X = Cl and F] were prepared as tetra-*n*-butylammoniun salts of formula Bu_4NHL by an adapted method employed to synthesize other oxamate salts.[3,4]

^1H and ^{13}C NMR spectra of the ligands were obtained with a Bruker AVANCE-III 400 Nanobay spectrometer. Chemical shifts (δ) are reported in ppm with $CDCl_3$ as the internal standard. IR spectra were recorded on a Perkin Elmer 882 spectrometer in the range 4000-400 cm^{-1} and a spectral resolution of 4 cm^{-1} by using dry KBr pellets (see Figs. S1-S3, ESI). Elemental analyses (C, H, N) were performed using a Perkin-Elmer 2400 analyzer. Thermogravimetric analysis (TG/DTA) were carried out with a Shimadzu TG/DTA 60 under a dinitrogen atmosphere at a heating rate of 10 °C min^{-1} from room temperature to 700 °C (Figs, S4-S11, ESI). X-ray powder diffraction patterns were done on a Rigaku / Geirgeflex diffractometer working at room temperature. Diffraction data were collected in the Bragg/Brentano mode (deg s^{-1}) using monochromatic Cu-Kα radiation. Simulated PXRD patterns of all lanthanides complexes are generated with the Mercury® software using the crystal data retrieved from the CIF (Figs. S12-S19, ESI). Direct current (dc) magnetic susceptibility and magnetization measurements for all compounds were performed on a Cryogenics SQUID magnetometer model S700. Alternating current (ac) magnetic susceptibility measurements for the gadolinium(III), dysprosium(III) and terbium(III) complexes were carried out with a Quantum Design

PPMS with an oscillating field of 5 Oe in the temperature and frequency ranges 2.0-10 K and 10-10 kOe respectively, under zero and non-zero applied dc fields. Both dc and ac magnetic measurements were performed on crushed samples placed in gelatin capsules with mineral oil to prevent the movement and orientation of the crystals. Diamagnetic corrections of the constituent atoms are estimated from Pascal's constants[5] as -628×10^{-6} (**1_F**), -630×10^{-6} (**2_F**), -633×10^{-6} (**3_F**), -631×10^{-6} (**4_F**), -661×10^{-6} (**1_Cl**), -630×10^{-6} (**2_Cl**), -666×10^{-6} (**3_Cl**) and -664×10^{-6} cm^3 mol^{-1} (**4_Cl**) [per lanthanide(III) ion]. Experimental magnetic susceptibilities are also corrected for the magnetization of the sample holder.

Synthesis of Bu$_4$NHL (X = Cl/F). Tetrabutylammonium hydroxide 40% in water (1.42 mL, 2.05 mmol) is added dropwise to an aqueous mixture (20.0 mL) of the proligand with X = Cl (466.6 mg, 2.05 mmol)/F (432.9 mg, 2.05 mmol).[1] The resultant solution is heated at 80 °C under continuous stirring for 1 h. Then, the solution is evaporated until it resulted into a yellow oil. Acetone is added to the oil to obtain the pasty solid that is filtered and washed with acetone. Yield: 91 (X = Cl) and 97% (X = F). Elemental analysis [exp. (calcd.)] for $C_{24}H_{41}ClN_2O_3$ (441.05 g mol^{-1}): C, 65.24 (65.36); H, 9.29 (9.37); N, 6.15 (6.35) %. ^{1}H NMR ($CDCl_3$, 400 MHz):δ 0.94 (t, 9H, *J* = 7.32; 3CH_3); 1.37 (sex, 8H, *J* = 7.28 Hz, 4CH_2); 1.60 (quin, 8H, *J* = 7.74 Hz, 4CH_2); 3.24 (t, 8H, *J* = 8.65 Hz, 4CH_2); 7.19 (d, 2H, *J* = 8.80 Hz, C–H_{ring}); 7.57 (d, 2H, *J* = 8.79 Hz, C–H_{ring}); 9.81 (s, 1H, N–H) ppm. ^{13}C NMR ($CDCl_3$, 400 MHz): δ 13.68 (CH_3); 19.76 (CH_2); 24.03 (CH_2); 58.83 (CH_2); 120.30 (C_{ring}), 128.12 (C_{ring}), 137.3 (C_{ring}), 163.15 (C=O), 163.7 (C=O) ppm. Selected IR bands (KBr, cm^{-1}): 3354 (ν_{NH}); 2960 and 2873 (ν_{CH}); 1653 ($\nu_{C=O}$); 1591 ($\nu_{C=C}$); 1367 ($\delta_{C\text{-}H}$), 1357 ($\delta_{C\text{–}N}$) cm^{-1}.

Elemental analysis [Exp. (Calcd.)] for $C_{26}H_{46}FN_2O_3$ (453.65 g mol^{-1}): C, 68.49 (68.84); H, 10.10 (10.22); N, 5.99 (6.18) %. ^{1}H NMR ($CDCl_3$, 400 MHz, δ 0.99 (t, 9H, *J* = 7.34; $3CH_3$); 1.43 (sex, 8H, *J* = 7.38 Hz, $4CH_2$); 1.65 (quin, 8H, *J* = 7.72 Hz, $4CH_2$); 3.3 (t, 8H, *J* = 8.00 Hz, $4CH_2$); 6.97 (t, 2H, *J* = 8.75 Hz, C−H$_{ring}$); 7.62 (dd, 2H, *J* = 4.90;9.08 Hz, C−H$_{ring}$); 9.83 (s, 1H, N−H) ppm. ^{13}C NMR ($CDCl_3$, 400 MHz):δ 13.71 (CH_3); 19.77 (CH_2); 24.06 (CH_2); 58.84 (CH_2); 115.23 and 115.45 (d C$_{ring}$); 120.48 and 120.56 (C$_{ring}$); 134.85 (C$_{ring}$); 157.60 (C$_{ring}$); 160.00 (C$_{ring}$); 163.09 (C=O); 163.87 (C=O) ppm. Selected IR bands(KBr): 3358 (ν_{NH}); 2960 and 2876 (ν_{CH}); 1692, 1646 ($\nu_{C=O}$); 1538 ($\nu_{C=C}$); 1388 ($\delta_{C\text{-}H}$), 1350 ($\delta_{C–N}$) cm^{-1}.

Synthesis of $Bu_4N[Ln(HL)_4(dmso)]\cdot nH_2O$ with Ln = Eu^{3+}, $Gd^{3+}$and Dy^{3+} and n = 3 (X = Cl) and 2 (X = F). An aqueous solution (3.0 mL) containing the corresponding lanthanide salt $Ln(CH_3COO)_3\cdot xH_2O$ (0.085 mmol) is added dropwise to a dmso solution (8.0 mL) of Bu_4NHL with X = Cl (150 mg, 0.34 mmol)/F (154 mg, 0.34 mmol) at room temperature. Then, the system is maintained at 70 °C for 5 min, filtered, added to a Petri dish, and left to stand at room temperature. X-ray quality crystals were grown after 5 days. They were collected and used for X-ray diffraction.

1_Cl: Yield 53%. Elemental analysis [exp. (calcd.)] for $C_{50}H_{68}Cl_4EuN_5O_{16}S$ (1320.94 g mol^{-1}): C 44.60 (45.37), H 5.10 (5.18), N 5.27 (5.29) %. IR (KBr, cm^{-1}): 3408, 3213, 3165, 3113, 3057, 2965, 2876, 1659, 1636, 1631, 1587, 1541, 1487, 1359, 1306, 1020, 1010, 837, 786, 490 cm^{-1}.

2_Cl: Yield: 52%. Elemental analysis [exp. (calcd.)] for $C_{50}H_{68}Cl_4GdN_5O_{16}S$ (1326.23 g mol^{-1}): C 44.50 (45.28), H 5.14 (5.17), N 5.20 (5.28) %. IR (KBr, cm^{-1}): 3419, 3192, 3165, 3113, 3058, 2965, 2874, 1697, 1658, 1636, 1629, 1586, 1541, 1488, 1358, 1306, 1023, 1008, 836, 786, 491 cm^{-1}.

3_Cl: Yield: 53%. Elemental analysis [exp. (calcd.)] for $C_{50}H_{68}Cl_4DyN_5O_{16}S$ (1331.48 g mol^{-1}): C 44.94 (45.10), H 5.08 (5.15), N 5.15 (5.26) %. IR (KBr, cm^{-1}): 3408, 3206, 3165, 3115, 3057, 2965, 2878, 1701, 1653, 1647, 1636, 1631, 1624, 1587, 1541, 1489, 1361, 1306, 1020, 1010, 837, 787, 490 cm^{-1}.

1_F: Yield: 51%; Elemental analysis [exp. (calcd.)] for $C_{50}H_{68}F_4EuN_5O_{16}S$ (1255.12 g mol^{-1}): C 47.59 (47.85), H 5.34 (5.58), N 5.40 (5.46)%. IR (KBr, cm^{-1}): 3410, 3229, 3192, 3144, 3073, 2967, 2876, 1697, 1661, 1633, 1605, 1549, 1505, 1362, 1308, 1032, 1015, 839, 802, 505, 502 cm^{-1}.

2_F: Yield: 48%. Elemental analysis [exp. (calcd.)] for $C_{50}H_{68}F_4GdN_5O_{16}S$ (1260.41 g mol^{-1}): C 47.04 (47.65), H 5.28 (5.44), N 5.45 (5.56)%. IR (KBr, cm^{-1}): 3439, 3225, 3192, 3144, 3075, 2968, 2878, 1697, 1659, 1636, 1605, 1549, 1505, 1362, 1308, 1032, 1011, 839, 804, 505, 501 cm^{-1}.

3_F: Yield: 57%. Elemental analysis [exp. (calcd.)] for $C_{50}H_{68}F_4DyN_5O_{16}S$ (1255.66 g mol^{-1}): C 47.07 (47.45), H 5.31 (5.42), N 5.60 (5.53)%.IR (KBr, cm^{-1}): 3492, 3227, 3192, 3144, 3073, 2967, 2876, 1697, 1661, 1633, 1605, 1549, 1505, 1362, 1308, 1032, 1015, 839, 802, 505, 502 cm^{-1}.

Synthesis of $Bu_4N[Tb(HL)_4(dmso)]\cdot 3H_2O$ with n = 3 (X = Cl) and 2 (X = F). An aqueous solution (3.0 mL) containing $TbCl_3\cdot H_2O$ (0.085 mmol) is added dropwise to a dmso solution (8.0 mL) of Bu_4NHL with X = Cl (150 mg; 0.34 mmol)/F (154 mg; 0.34 mmol) at room temperature. Then, the system is maintained at 70 °C for 5 min, filtered, added to a Petri dish, and left to stand at room temperature. Single crystals were formed after 5 days. They were collected and used for X-ray diffraction.

4_Cl: Yield: 55%. Elemental analysis [exp. (calcd.)] for $C_{50}H_{68}Cl_4TbN_5O_{16}S$ (1327.90 g mol^{-1}): C 44.98 (45.22), H 5.07 (5.16), N 5.15 (5.27)%. IR (KBr, cm^{-1}): 3398, 3209, 3167, 3116, 3062, 2964, 2875, 1699, 1661, 1636, 1587, 1541, 1481, 1362, 1306, 1020, 1010, 837, 786, 490 cm^{-1}.

4_F: Yield: 52%. Elemental analysis [exp. (calcd.)] for $C_{50}H_{68}F_4TbN_5O_{16}S$ (1262.08 g mol^{-1}): C 46.89 (47.58), H 5.41 (5.43), N 5.45 (5.55)%. IR (KBr, cm^{-1}): 3416, 3229, 3194, 3144, 3075, 2967, 2876, 1697, 1660, 1635, 1603, 1549, 1505, 1361, 1306, 1030, 1011, 839, 804, 507, 501 cm^{-1}.

Single Crystal X-ray Diffraction. Single crystal X-ray diffraction data were collected on either a Bruker-AXS Kappa Duo diffractometer with an APEX II CCD detector (Cu Kα or Mo Kα radiation, 296 K) or an Oxford Gemini A-Ultra diffractometer equipped with an Atlas CCD detector (Mo Kα radiation, 220 or 250 K). Bruker programs SAINT and SADABS[6] and the Oxford ones CrysAlis CCD and CrysAlisRED[7] were used for cell refinement and data indexing, integration, and reduction. Multi-scan absorption correction was performed for all datasets.[8] Structure solution was carried out by using SHELXL-2014[9] or SUPERFLIP[10] within the WinGX.[11] All refinements were done with SHELXL.[9] Structure analysis and artwork preparation were performed with Mercury[12] and ORTEP-3.[13] Non-hydrogen and hydrogen atoms were refined anisotropically and isotropically, respectively. All hydrogen atoms bound to the carbon atoms were added to their corresponding carbons following a riding model with fixed bond lengths and angles. In the case of N-H and water hydrogen atoms, before their constraining, they were firstly found from the difference Fourier map and checked for suitable directionality of hydrogen bonds. Hydrogen atoms had their isotropic atomic displacement parameters were set to $1.2U_{iso}$(C/N) or $1.5U_{iso}$(O). The complete X-ray diffraction dataset for all structures is available under CCDC number codes which are shown in Table 1 togeheter with a summary of the crystallographic data and refinement conditions.

Photoluminescence studies. All the luminescence measurements were recorded using a Jobin-Yvon Model Fluorolog FL3-22 spectrophotometer, equipped with a R928 Hamamatsu photomultiplier and 450 W xenon lamp as an excitation source. The spectra were corrected with respect to the Xe lamp intensity and spectrometer response. Measurements of emission decay were performed with the same equipment, by using a pulsed Xe (3μs bandwidth) source. The experimental intensity parameters, Ω_λ ($\lambda = 2$ and 4) for the Eu^{3+} complexes were obtained using the Eq. 1 and the respective emission spectra:[14]

$$\Omega_\lambda = \frac{3\hbar c^3 A_{0\to J}}{4e^2\omega^3\chi\left\langle {}^7F_J \left\| U^{(\lambda)} \right\| {}^5D_0 \right\rangle^2} \qquad (1)$$

The squared reduced matrix element in Eq. 1 is given by $\left\langle {}^7F_J \left\| U^{(\lambda)} \right\| {}^5D_0 \right\rangle^2$, assuming values of 0.0032 and 0.0023 for the $^5D_0 \rightarrow {}^7F_2$ and 0.0023 for the $^5D_0 \rightarrow {}^7F_4$ transitions, respectively. These matrix elements were experimentally calculated by Carnall and collaborators, in the f-f transitions intensities analysis, and can be found in extensive tables.[14] Additionally, χ is the Lorentz local field correction term, given by $\chi = n(n+2)^2/9$, in order to account for local-field effects on the optical properties of material.[15] The refractive index (n) has been assumed equal to 1.5, an average index of refraction obtained for the lanthanide complexes in the solid-state. It is important to emphasize that, in the present study, the experimental Ω_6 parameter could not be estimated because the $^5D_0 \rightarrow {}^7F_6$ transition was not observed experimentally. The spontaneous emission coefficients ($A_{0\lambda}$), [$A_{01} = 0.31 \times 10^{-11}(n)^3(\nu_{01})^3$], were obtained by means of Eq. 2, with the approximate value of 50 s^{-1}, considering the refractive index (n) defined above.[16]

$$A_{0\lambda} = \frac{v_{01}}{v_{0\lambda}} \frac{S_{0\lambda}}{S_{01}} \left(A_{01}\right) \qquad (2)$$

The $A_{0\lambda}$ term in Eq. 2 represents the spontaneous emission coefficients of the $^5D_0 \rightarrow {}^7F_2$ and $^5D_0 \rightarrow {}^7F_4$ transitions (for λ = 2 and 4, respectively), and they can be calculated from the $^5D_0 \rightarrow {}^7F_1$ magnetic dipole transition, which acts as a reference transition. This transition is practically insensitive to the changes of the chemical environment. S_{01} and $S_{0\lambda}$ are the calculated areas under the curves of the $^5D_0 \rightarrow {}^7F_1$ and $^5D_0 \rightarrow {}^7F_\lambda$ transitions, with the respective ν_{01} and $\nu_{0\lambda}$ being their energy barycenters. The experimental quantum efficiencies values (η) were obtained through Eq. (3), considering ($A_{total} = 1/\tau = A_{rad} + A_{nrad}$), where τ is to the lifetime decay, A_{rad} and A_{nrad} are radiative and non-radiative rates.[17]

$$\eta = \frac{A_{rad}}{A_{rad} + A_{nrad}} \qquad (3)$$

Theoretical Study Procedure

*1- Ground State Geometry Calculation of **1_F** and **1_Cl** complexes*

Currently, the ground state geometries of lanthanide compounds can be calculated from two different approaches. The first one would be *ab initio* and DFT methods associated with an effective core potential (ECP),[18] and the second one would deal with semiempirical methods.[19,20,21] The first approach has a greater acceptance of the scientific community working with theoretical methods. For this reason, in 2005, at the time of the improvement of the latest Sparkle model parameterized for the AM1 semiempirical method,[22] a tremendous computational effort was done trying to prove that when it comes to predicting the ground state geometry of coordination compounds composed by lanthanide ions. The Sparkle/AM1 model has an accuracy similar to that presented by the best *ab initio* methodologies, however, with a significantly lower computational cost. Several models have been developed since 2006 such as Sparkle/PM3 (2006-2009),[23,24] Sparkle/PM6 (2010),[25] Sparkle/PM7 (2013),[26] Sparkle/RM1 (2013),[27] and finally, a new approach in which the lanthanide ion has orbitals which call RM1 model to trivalent lanthanides. In 2011, we showed that not only the Sparkle/AM1 model has similar accuracy to the best methodologies *ab initio*, but also the Sparkle/PM3 and Sparkle/PM6 models.[28] In several recent studies, we observed that although all these semiempirical models developed to treat systems containing lanthanide exhibit similar accuracy, it is thus crucial to justify the chosen model. For this reason, both systems have been optimized using the Sparkle/AM1, Sparkle/PM3, Sparkle/PM6, Sparkle/PM7, Sparkle/RM1, and RM1 models. Subsequently, the calculated systems were superimposed with their respective crystallographic systems to obtain the associated error, aiming at choosing which of the methods presented the smallest error to be used in the calculations of the luminescent properties. Tables S6 and S7 show that the Sparkle/PM6 and Sparkle/RM1 methods presented the highest accuracy for the system optimizations of **1_F** and **1_Cl**, respectively. For this reason, these methods were chosen to proceed with the calculations of the luminescent properties. Figures S28 and S29 show the overlap of the crystallographic structures with the calculated structures of **1_F** and **1_Cl**, respectively.

2- *Excited-state calculations*

The calculations of the singlet and triplet excited state energies were performed using the INDO/S-CIS method[29,30] (*Intermediate Neglect of Differential Overlap/ Spectroscopic -*

Configuration Interaction Single) implemented in the ORCA program.[31] The calculated ground state geometry was used as input. We have used a point charge of +3e to represent the trivalent lanthanide ion.

3- *Judd-Ofelt Intensity Parameters*

The intensity parameters were calculated from the Judd-Ofelt theory.[32,33] To get them, the QDC oneness models[34] implemented in LUMPAC program was employed.[35] This model is based on setting three parameters (Q, D and C) which are associated with the electron densities and the super delocalizabilities of the atoms of the coordination polyhedron. This model uses the Judd-Ofelt theory, and the intensity parameters were obtained by fitting the charge factors (g) and polarizabilities (α) associated to each of the Eu^{3+} - ligand atom bonds.

In this theory, the ion is affected by the nearest neighbor atoms, while the intensity parameters describe the interaction between the lanthanide ion and ligand atoms and are calculated by Eq. (4):

$$\Omega_{\lambda} = \left(2\lambda + 1\right) \sum_{t=\lambda-1}^{\lambda+1(odd)t} \sum_{p=-t}^{(all)} \frac{\left|B_{\lambda tp}\right|^{2}}{(2t+1)} \tag{4}$$

It is important to know the values that each variable paramerer λ, t and p can assume in relation to the others. The $B_{\lambda tp}$ parameter, in Equation 4, is calculated by adding two terms [Eq. (5)]

$$B_{\lambda tp} = B_{\lambda tp}^{ed} + B_{\lambda tp}^{dc} \tag{5}$$

In this last equation, the first term refers to the forced electric dipole contribution and its value is calculated by Eq. (6). The second term concerns to the dynamic coupling contribution and it is given by Eq. (7).

$$B_{\lambda tp}^{ed} = \frac{2}{\Delta E}\left\langle r^{t+1}\right\rangle \theta(t,\lambda)\gamma_{p}^{t} \tag{6}$$

$$B_{\lambda tp}^{dc} = -\left[\frac{(\lambda+1)(2\lambda+3)}{2\lambda+1}\right]^{1/2} \left\langle r^{\lambda}\right\rangle \left(1-\sigma_{\lambda}\right)\left\langle f\left\|C^{(\lambda)}\right\|f\right\rangle \Gamma_{p}^{t}\delta_{t,\lambda+1} \tag{7}$$

ΔE is in Eq (6) is given by the energy difference between the ground state barycenter and the first excited state configuration of opposite parity. The radial integrals, (r^{λ}), were taken from the literature.[36] The terms $\theta(t,p)$ are estimated from radial integrals of Hartree-Fock and correspond to the numeric factors associated with each trivalent lanthanide. The parameter γ_p^t is called field ligand and it is given by Eq (8):

$$\gamma_p^t = \left(\frac{4\pi}{2t+1}\right)^{1/2} e^2 \sum_j \rho_j \left(2\beta_j\right)^{t+1} \frac{g_j}{R_j^{t+1}} Y_p^{t*}(\theta_j,\phi_j) \tag{8}$$

The term $Y_p^{t*}(\theta_j,\phi_j)$ corresponds to the conjugated spherical harmonics. This term formalizes that crystal field Hamiltonian and it is calculated as a function of the charge density between the trivalent europium ion and the j ligand atoms. More details can be seen in the literature.[37,38]

The term $\left(1-\sigma_{\lambda}\right)$ in Eq (7) is related to the shielding field due to the orbitals, which have a radial extension larger than those of the 4f orbitals. The parameters $\left\langle f\left\|C^{(\lambda)}\right\|f\right\rangle$ are a tensor operator of rank and they are determined according to the value assumed term λ, for λ = 2, 4 and 6. The parameter Γ_p^t depends on the coordination geometry and the chemical environment around the lanthanide ion. It obeys to Eq. (9):

$$\Gamma_p^t = \left(\frac{4\pi}{2t+1}\right)^{1/2} \sum_j \frac{\alpha_j}{R_j^{t+1}} Y_p^{t*}(\theta_j,\phi_j) \tag{9}$$

It is necessary to calculate the values of the γ_p^t and Γ_p^t parameters because the charge factor (g) and polarizabilities (α) no feature well established analytical equations. Thus, the methodology used to determine the intensity parameters is based on the adjustment of these two quantities to minimize the error between the theoretical and the experimental Ω_2 and Ω_4 parameters.

4- *Energy transfer and back-transfer rates*

The rates of energy transfer between the ligands and the lanthanide ion are calculated based on the model developed by Malta and collaborators.[39,40] Thus, the energy transfer rates are given by Eq. (10).

$$W_{ET} = W_{ET}^{mm} + W_{ET}^{em} \tag{10}$$

The W_{ET}^{mm} term corresponds to the energy transfer rate obtained from the multipolar mechanism and it is given by Eq. (11):

$$W_{ET}^{mm} = \frac{2\pi}{\hbar}\frac{e^2 S_L}{(2J+1)G} F \sum_{\lambda} \gamma_\lambda \left\langle \alpha' J' \middle\| U^{(\lambda)} \middle\| \alpha J \right\rangle^2 + \frac{4\pi}{\hbar}\frac{e^2 S_L}{(2J+1)GR_L^6} F \sum_{\lambda} \Omega_\lambda^{ed} \left\langle \alpha' J' \middle\| U^{(\lambda)} \middle\| \alpha J \right\rangle^2 \tag{11}$$

The Ω_λ^{ed} term in this last equation represents the electric dipole contributions to the intensity parameters, where $\left\langle \alpha' J' \middle\| U^{(\lambda)} \middle\| \alpha J \right\rangle$ are elements of the reduced matrix, J is the total quantum number of the angular momentum of the lanthanide ion, G is the degeneration of the initial state of the ligand and S_L is the dipolar force. The γ_λ parameter is calculated by Eq. (12) and F contains the sum of the Frank Condon factors, being that is given by Eq. (13).

$$\gamma_\lambda = (\lambda+1)\frac{\left\langle r^\lambda \right\rangle^2}{\left(R_L^{\lambda+2}\right)^2}\left\langle 3 \middle\| C^{(\lambda)} \middle\| 3 \right\rangle^2 \left(1-\sigma_\lambda\right)^2 \tag{12}$$

$$F = \frac{1}{\hbar\gamma_L}\sqrt{\frac{\ln 2}{\pi}}\exp\left[-\left(\frac{\Delta}{\hbar\gamma_L}\right)^2 \ln 2\right] \tag{13}$$

The $\hbar\gamma_L$ factor is the bandwidth of the ligand state and Δ is the energy difference between the donor and acceptor state involved in the energy transfer process.

The second term in Eq. (10), W_{ET}^{em}, refers to the energy rates obtained from the exchange mechanism and are calculated by Eq. (14):

$$W_{ET}^{em} = \frac{8\pi}{3\hbar}\frac{e^2\left(1-\sigma_0\right)^2}{\left(2J+1\right)R_L^6} F \left\langle \alpha' J' \middle\| S \middle\| \alpha J \right\rangle^2 \sum_m \left| \left\langle \varphi \middle| \sum_k \mu_Z\left(k\right) s_m\left(k\right) \middle| \varphi' \right\rangle \right|^2 \tag{14}$$

s_m is the spherical component of the spin operator, μ_z is the z component of the dipole operator and S is the total spin operator of the lanthanide ion. The distance between the donor and acceptor state (R_L) is given by Eq. (15):

$$R_L = \frac{\sum_i c_i^2 R_i}{\sum_i c_i^2} \tag{15}$$

The energy transfer rates, W_{BT} , are obtained by multiplying the transfer rate (W_{ET}) by the Boltzmann factor, $\exp\left(-|\Delta|/k_B T\right)$, where Δ refers to the energy difference between the donor and acceptor levels and k_B is the constant of Boltzmann.

5- *Radiative and non- radiative emission rate, and emission quantum yield calculations*

The radioactive emission rate takes into account the magnetic dipole and forced electric dipole mechanisms. It is given by Eq. 16:

$$A\left({}^5D_0 - {}^7F_J\right) = \frac{64\pi^4\upsilon^3}{3h\left(2J+1\right)}\left[\frac{n\left(n^2+2\right)^2}{9}S_{ed} + n^3 S_{md}\right] \tag{16}$$

In this equation, υ is the energy difference between the states ${}^5D_0$ and ${}^7F_J$, h the Plank constant, $2J+1$ is the degeneration of the initial state, and n is the refractive index of the medium (generally a value of 1.5 is used). The S_{ed} (Eq (17) and S_{md} (Eq, 18) terms are the mechanisms of a forced electric dipole and magnetic dipole, respectively.

$$S_{ed} = e^2 \sum_{\lambda=2,4,6} \Omega_\lambda \left|\left\langle {}^5D_0 \left\| U^{(\lambda)} \right\| {}^7F_J \right\rangle\right|^2 \tag{17}$$

$$S_{md} = \frac{\mathrm{h}^2}{4mc^2}\left\langle J' \left\| L + 2S \right\| J \right\rangle^2 \tag{18}$$

The ${}^5D_0 \rightarrow {}^7F_J$ transitions (J = 0, 3, and 5) are forbidden by the forced electric dipole and the magnetic dipole mechanisms; that is, their contributions are equal to 0. Therefore, the contributions of these transitions to the rate of the radiative emission are calculated by Eq. (19) and are named branch proportions ($\beta_{0,J}$):

$$\beta_{0,J} = \frac{A_{0,J}}{A_{rad}} \tag{19}$$

The non-radiative emission rate (A_{nrad}) cannot yet be theoretically calculated. However, it can be obtained by Eq. (20) using the A_{rad} and the experimental lifetime:

$$\frac{1}{\tau} = A_{rad} + A_{nrad} \tag{20}$$

The quantum emission yield (A_{rad}) which is defined as the ratio between the light emitted and absorbed, is calculated by Eq. (21):

$$q = \frac{A_{rad}\eta_{^5D_0}}{\varphi\eta_{S_0}} \tag{21}$$

$\eta_{^5D_0}$ is the population of the $^5D_0$ level which depends on A_{nrad}. The η_{S_0} and ϕ terms correspond to the population at the singlet level and absorption rate, respectively. The values of the η_J levels are obtained through Eq. (22):

$$\frac{d\eta_j}{dt} = -\left(\sum_{i\neq j} W_{ji}\right)\eta_j + \sum_{i\neq j} W_{ji}\eta_i \tag{22}$$

Magnetic Properties

The europium(III) ions have a $4f^6$ electronic configuration and ^7F as a spectroscopic term. The spin-orbit coupling splits this ground term into seven states. The ground state, $^7F_0$, is nonmagnetic, but there is a magnetic excited state $^7F_1$ at about 300 cm^{-1} that can be thermally populated. At the low-temperature limit, the value of the $\chi_M T$ is zero because only the nonmagnetic ground state is populated. When the temperature increases, the first excited state became occupated, and the paramagnetism is observed.[41,42] Using these central ideas, Kahn and coworkers developed a model that is used herein to fit the $\chi_M T$ *vs.* T curves of **1_Cl** and **1_F** (Eq. 23).[42] These curves are shown in the ESI (Fig. S21).

$$\chi_M = \frac{N\beta^2}{3kTx}\,\frac{24 + (27x/2 - {}^{3}\!/2)e^{-x} + (135x/2 - {}^{5}\!/2)e^{-3x} + (189x - {}^{7}\!/2)e^{-6x} + (405x - {}^{9}\!/2)e^{-}}{1 + 3e^{-x} + 5e^{-3x} + 7e^{-6x} + 9e^{-10x} + 11e^{-}} \tag{23}$$

with

$$x = \frac{\lambda}{kT} \tag{24}$$

χ_M is the molar magnetic susceptibility, N is the Avogadro constant, β is the Bohr magneton, k is the Boltzmann constant, T is the temperature, λ is the spin-orbit coupling.

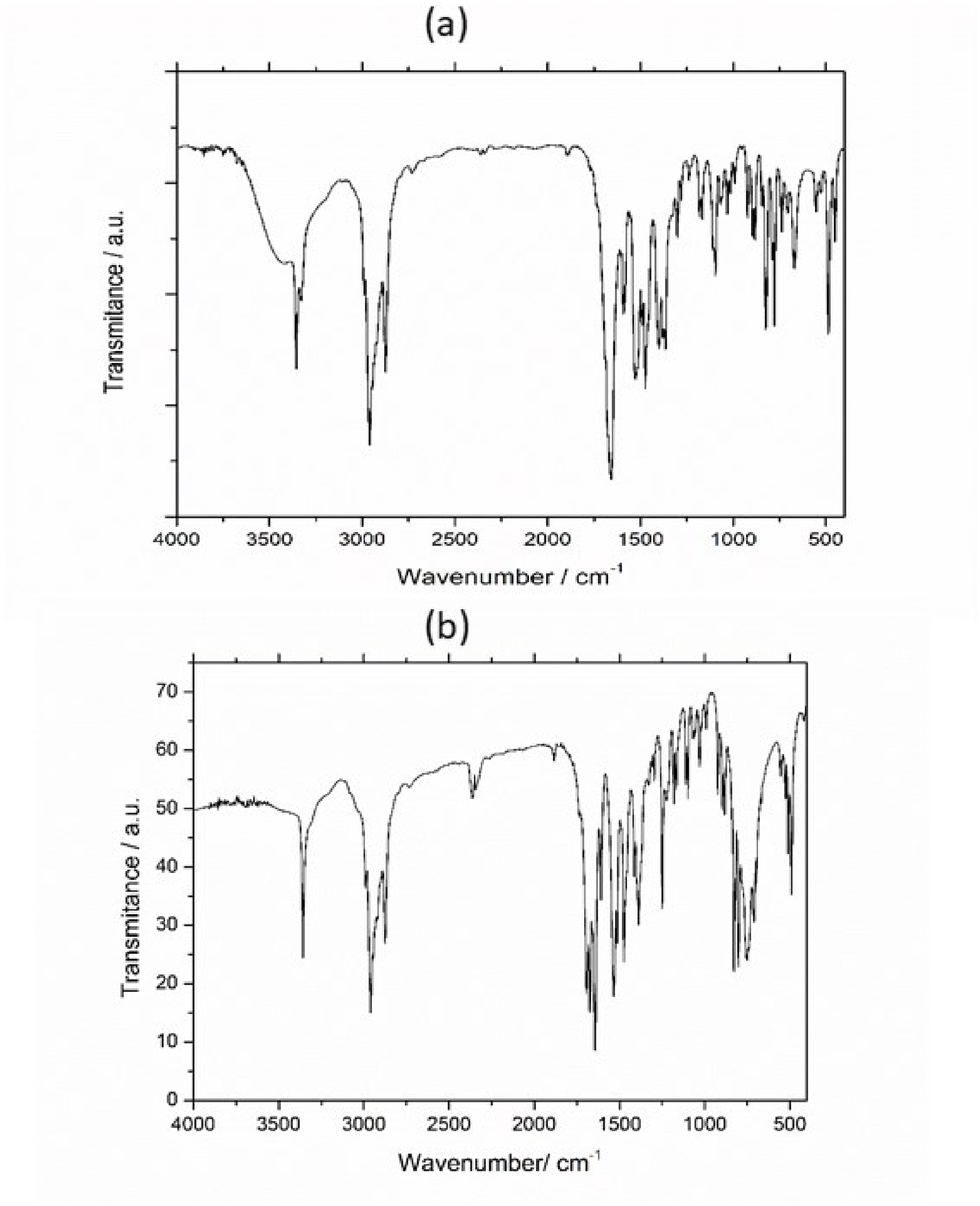

Fig. S1. IR spectra of Bu_4NHL with X = Cl (a) and F (b).

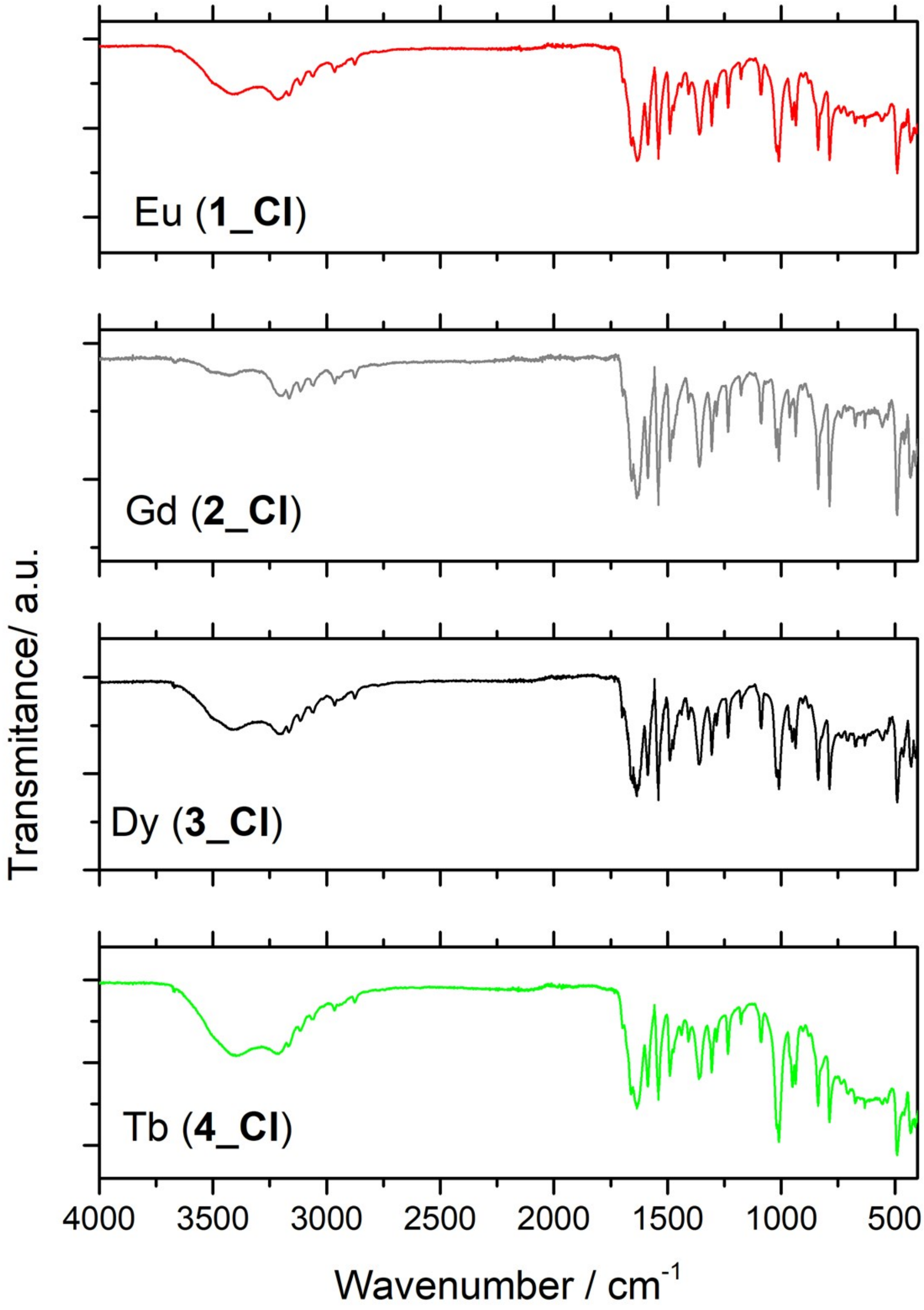

Fig. S2. IR spectra of **1_Cl**, **2_Cl**, **3_Cl**, and **4_Cl**.

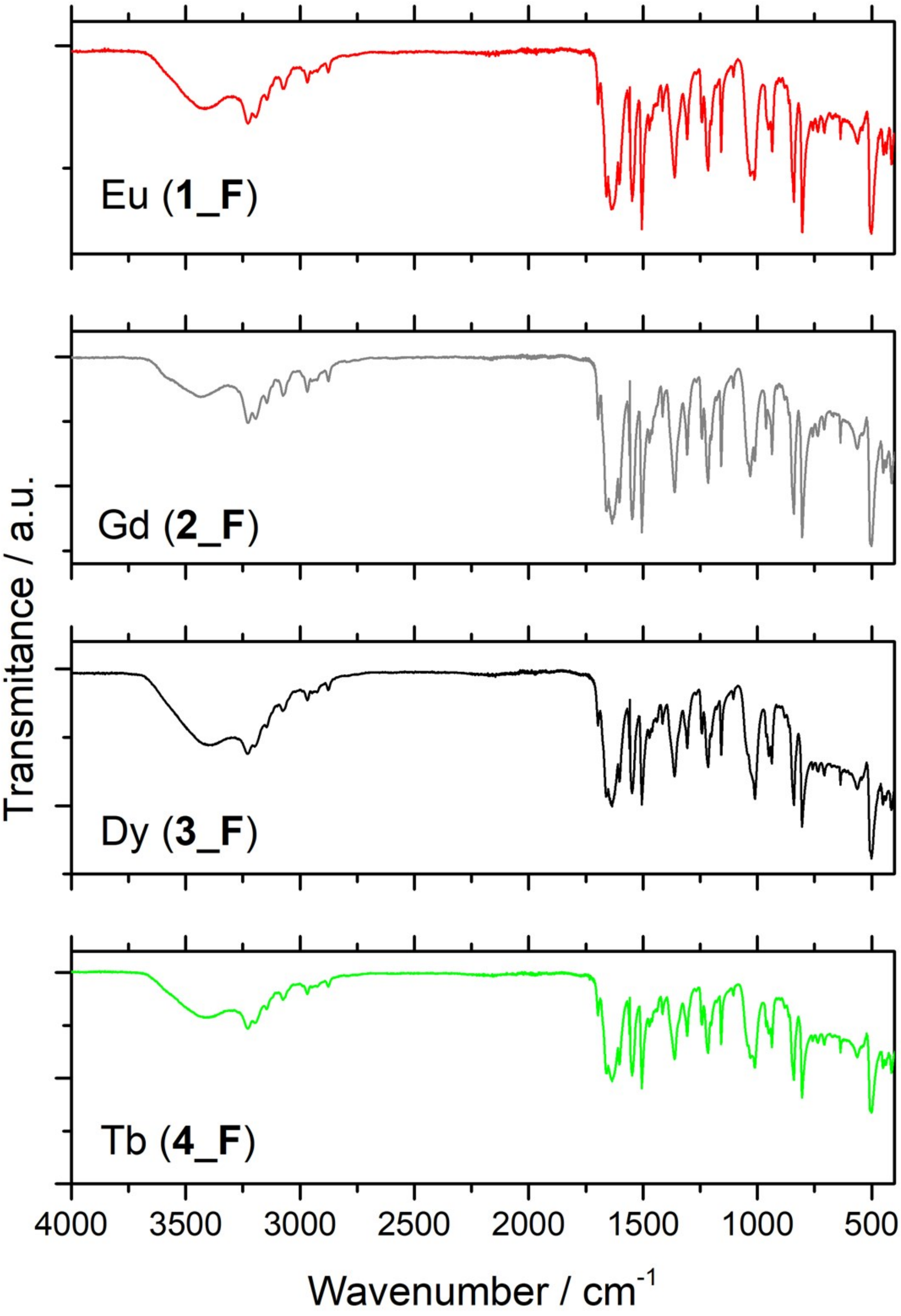

Fig. S3. IR spectra of **1_F**, **2_F**, **3_F,** and **4_F**.

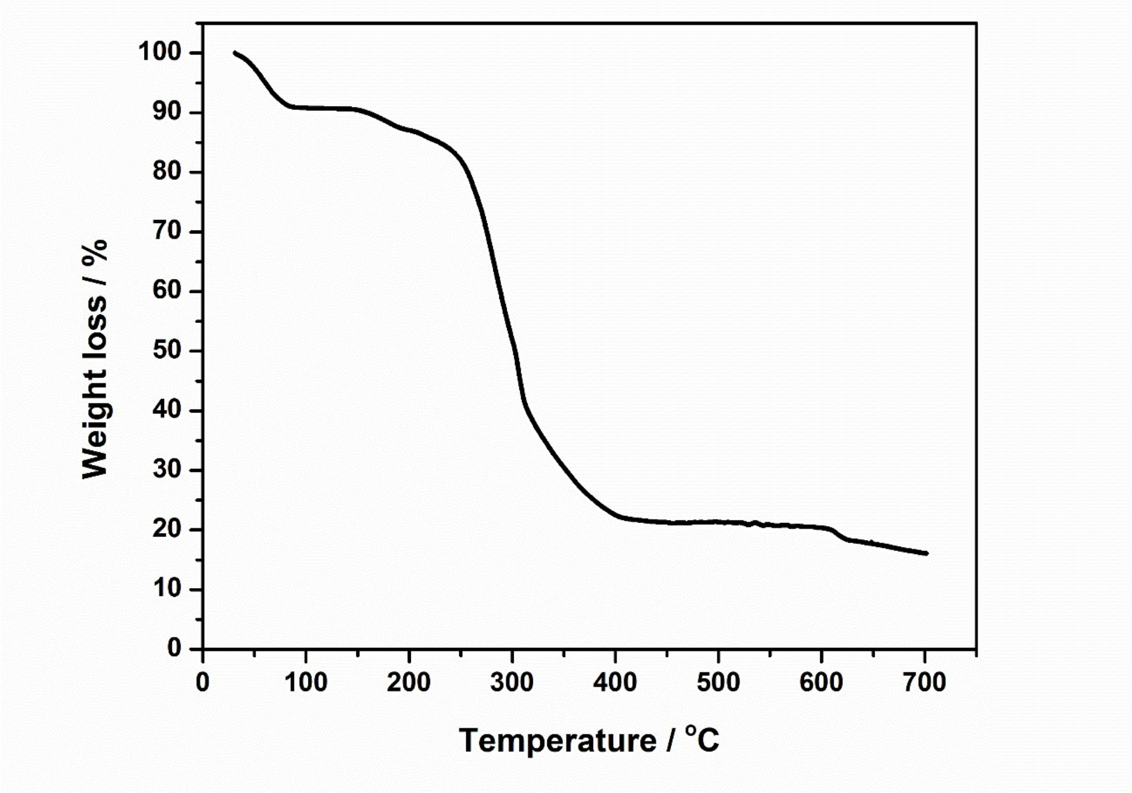

Fig. S4. TGA curve of **1_Cl**. Nitrogen flow (50 mL min^{-1}) at a heating rate of 10 ºC min^{-1}.

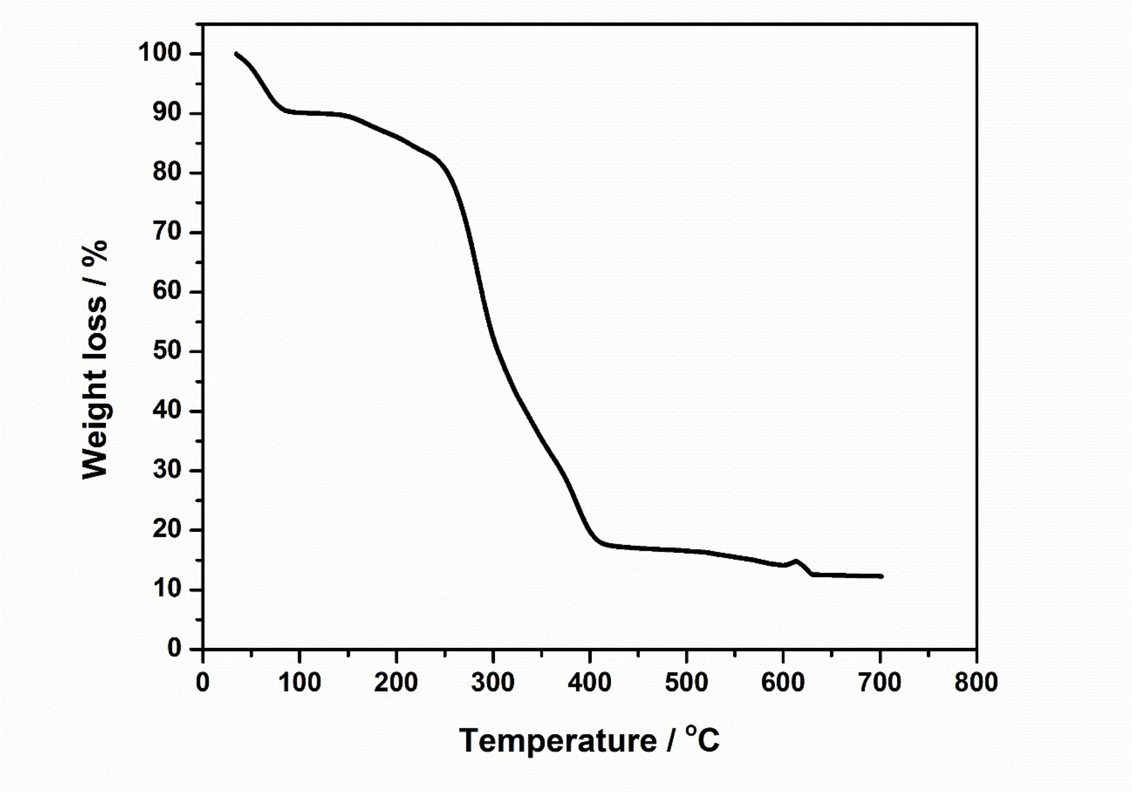

Fig. S5. TGA curve of **2_Cl**. Nitrogen flow (50 mL min^{-1}) at a heating rate of 10 ºC min^{-1}.

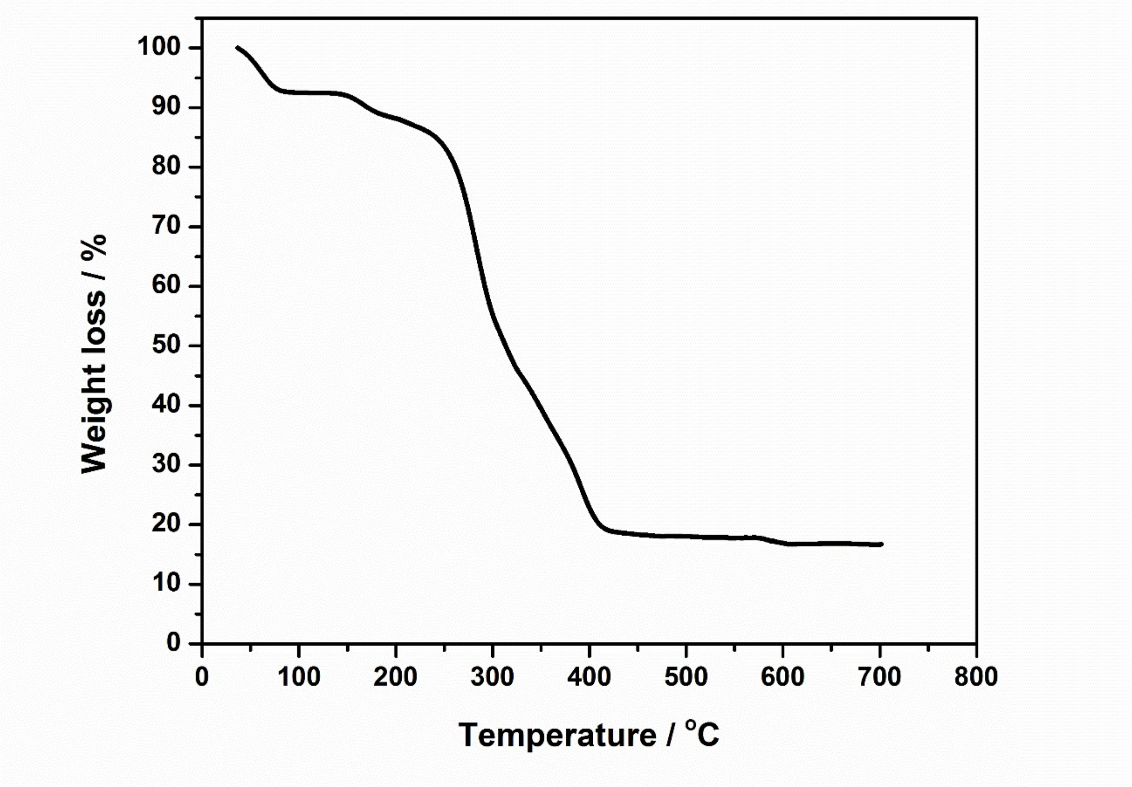

Fig. S6. TGA curve of **3_Cl** bulk. Nitrogen flow (50 mL min^{-1}) at a heating rate of 10 ºC min^{-1}.

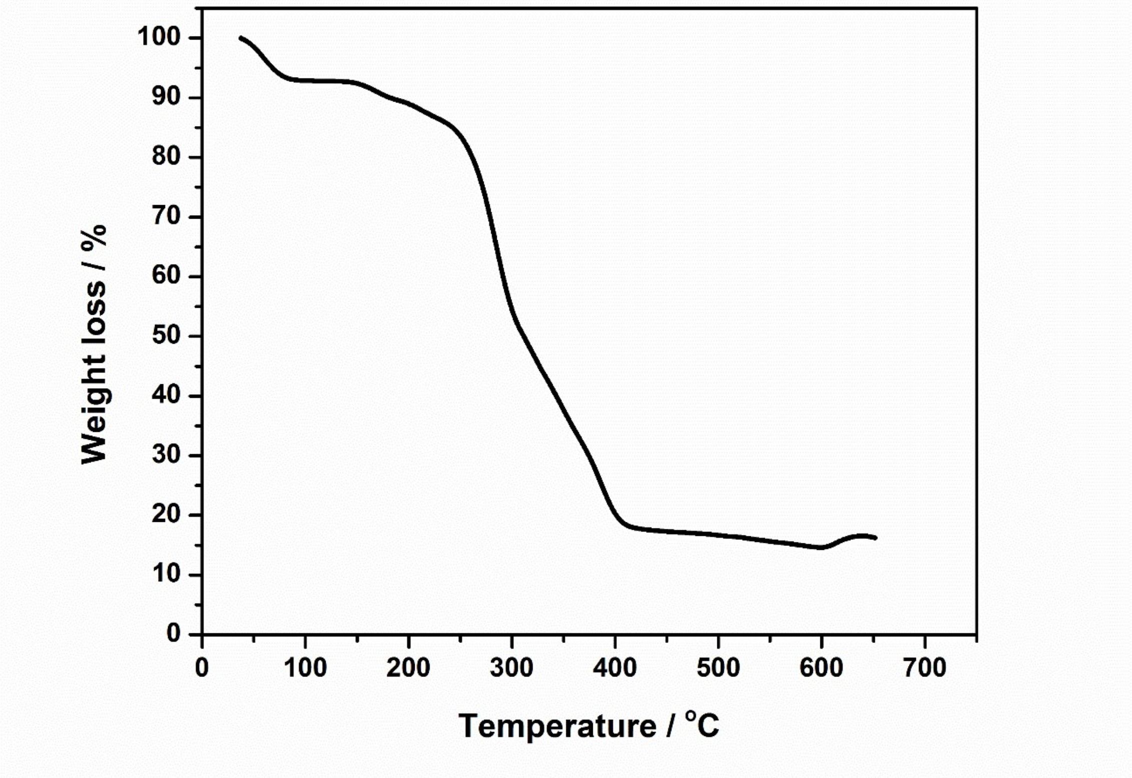

Fig. S7. TGA curve of **4_Cl**. Nitrogen flow (50 mL min^{-1}) at a heating rate of 10 ºC min^{-1}.

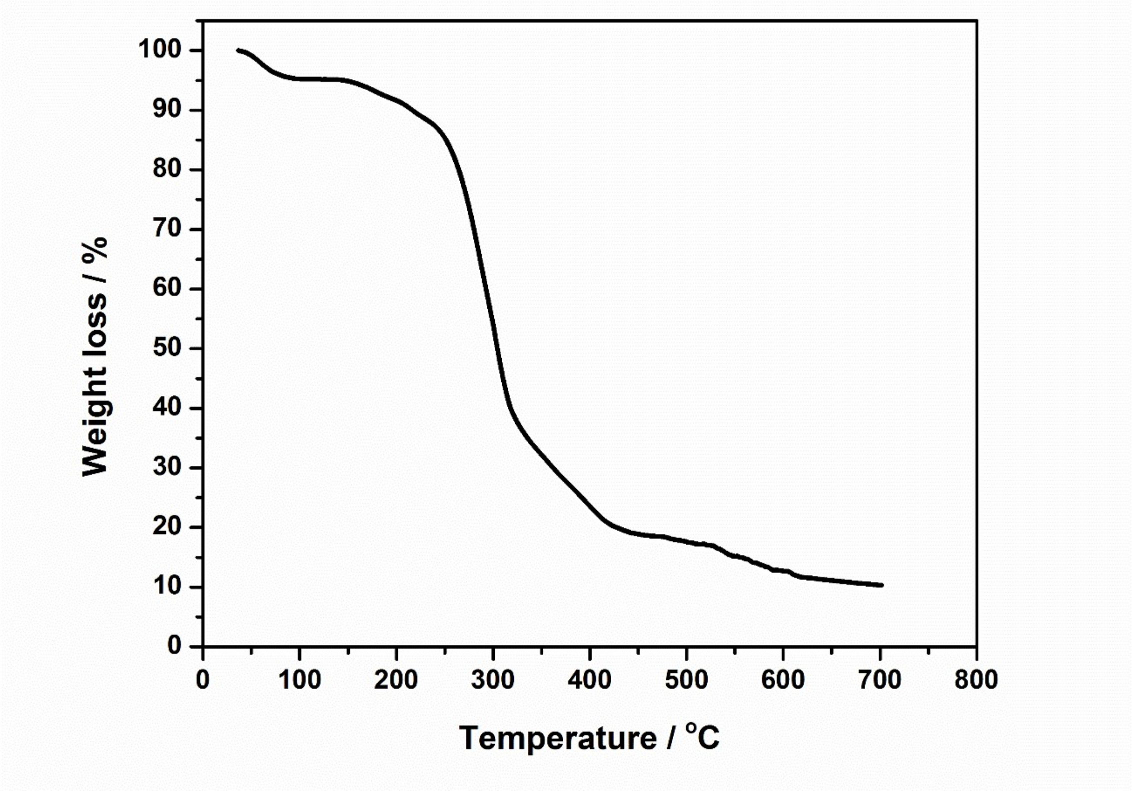

Fig. S8. TGA curve of **1_F**. Nitrogen flow (50 mL min^{-1}) at a heating rate of 10 ºC min^{-1}.

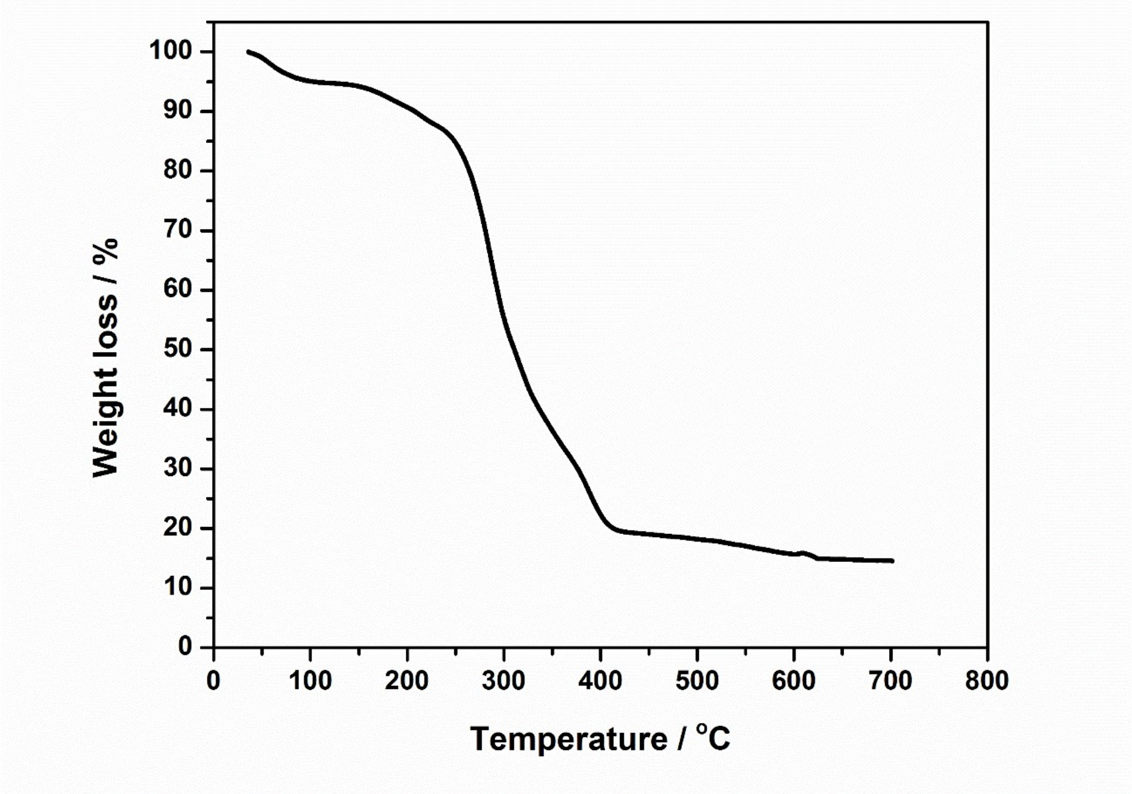

Fig. S9. TGA curve of **2_F**. Nitrogen flow (50 mL min^{-1}) at a heating rate of 10 ºC min^{-1}.

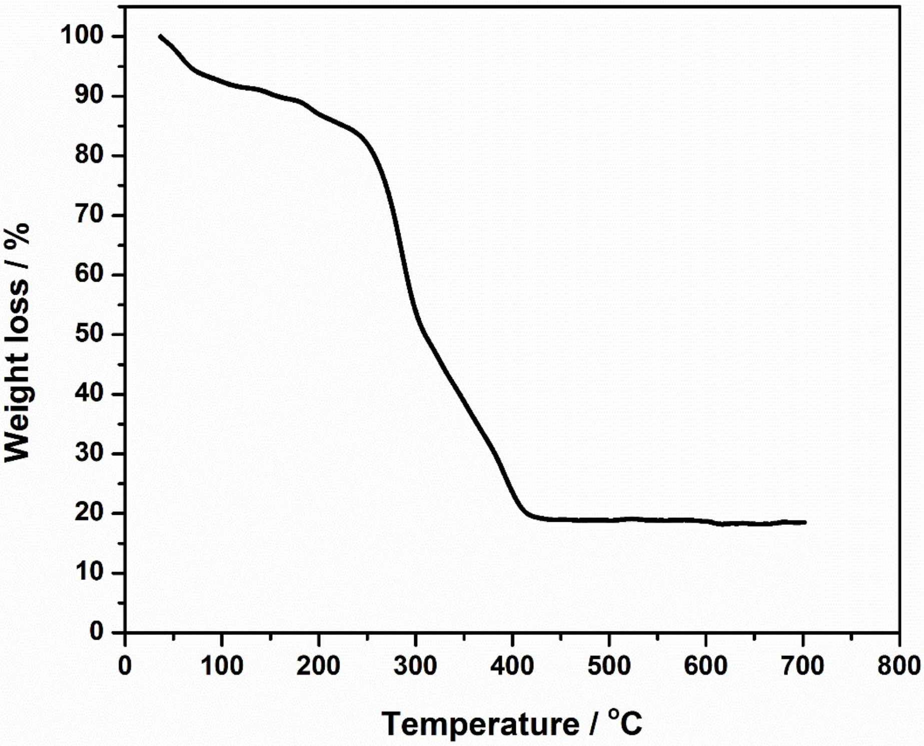

Fig. S10. TGA curve of **3_F**. Nitrogen flow (50 mL min^{-1}) at a heating rate of 10 ºC min^{-1}.

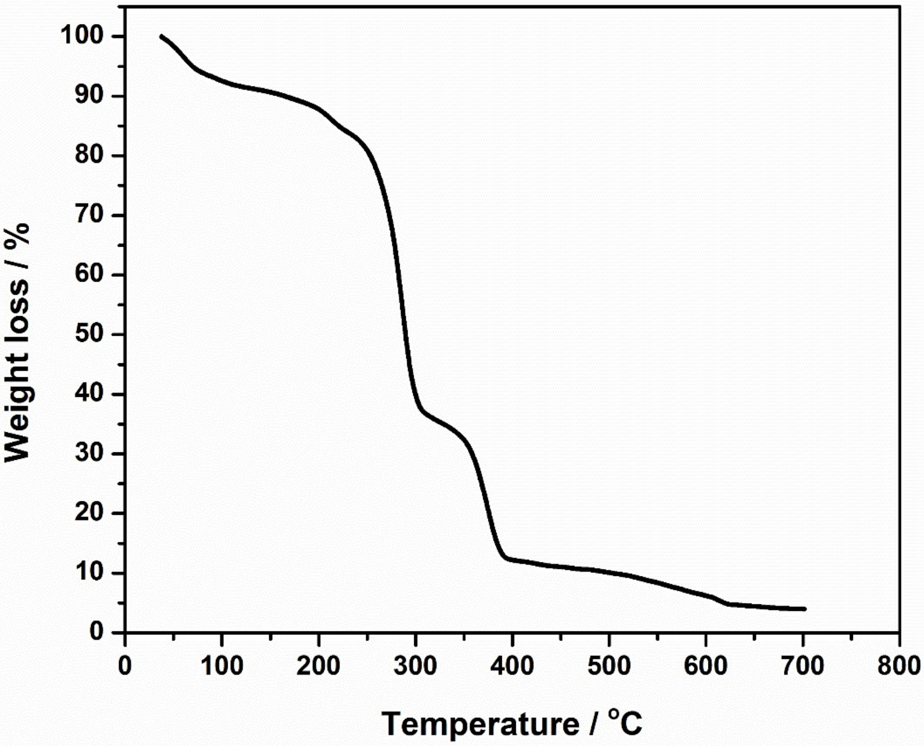

Fig. S11. TGA curve of **4_F**. Nitrogen flow (50 mL min^{-1}) at a heating rate of 10 ºC min^{-1}.

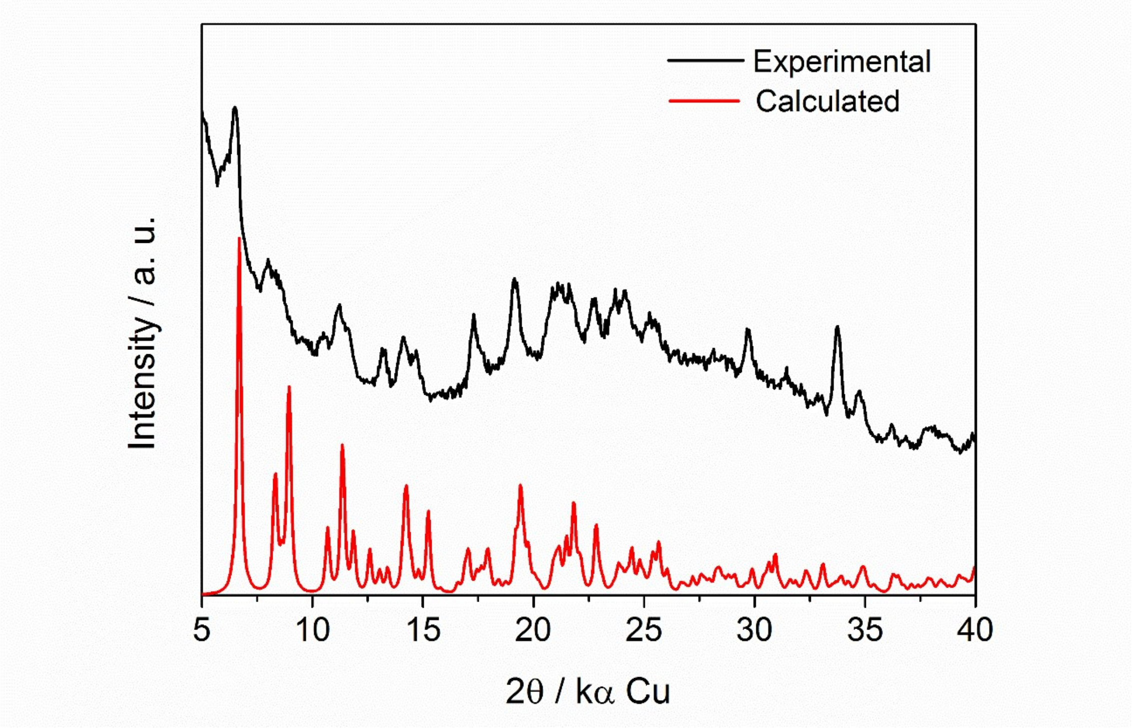

Fig. S12. X-ray diffraction patterns for **1_Cl**. Experimental (black line): powder diffraction of the bulk. Calculated (red line): simulation from single-crystal results employing the Mercury® software.

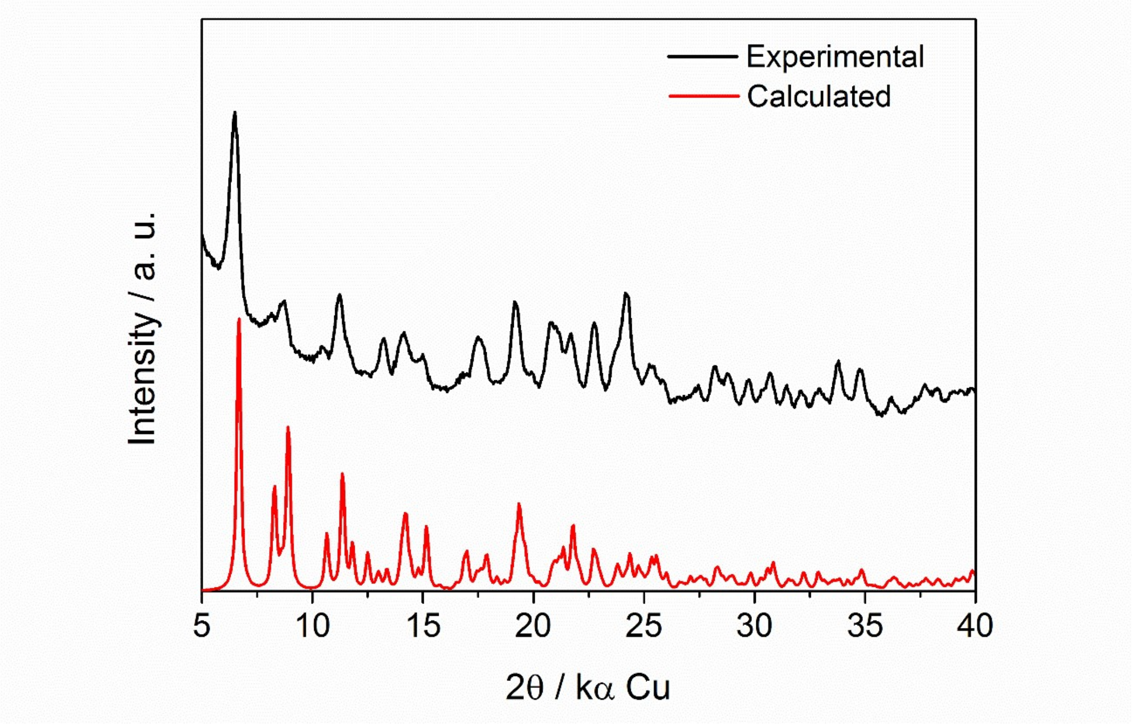

Fig. S13. X-ray diffraction patterns for **2_Cl**. Experimental (black line): powder diffraction of the bulk. Calculated (red line): simulation from single-crystal results employing the Mercury® software.

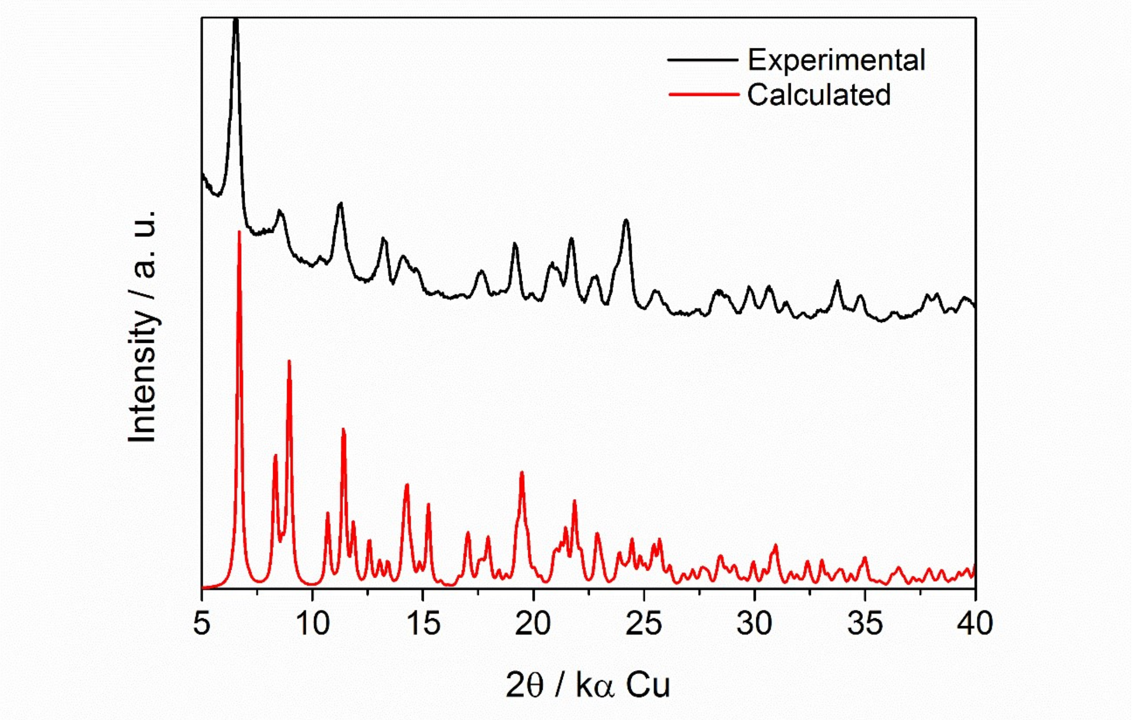

Fig. S14. X-ray diffraction patterns for **3_Cl**. Experimental (black line): powder diffraction of the bulk. Calculated (red line): simulation from single-crystal results employing the Mercury® software.

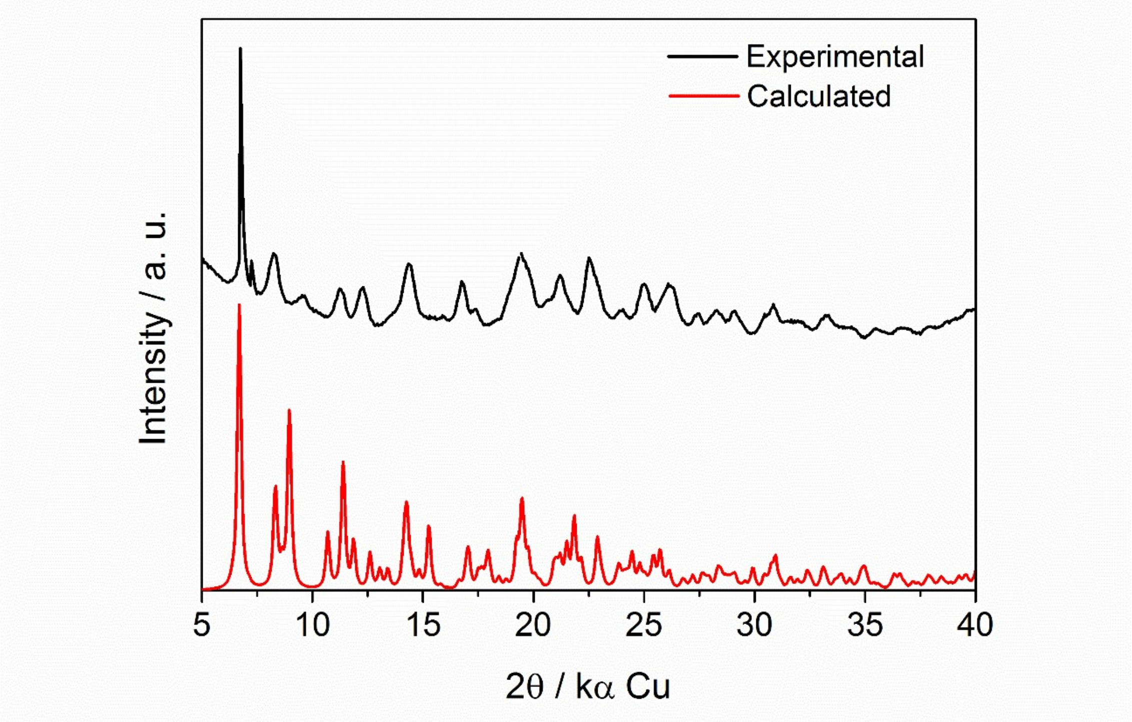

Fig. S15. X-ray diffraction patterns for **4_Cl**. Experimental (black line): powder diffraction of the bulk. Calculated (red line): simulation from single-crystal results employing the Mercury® software.

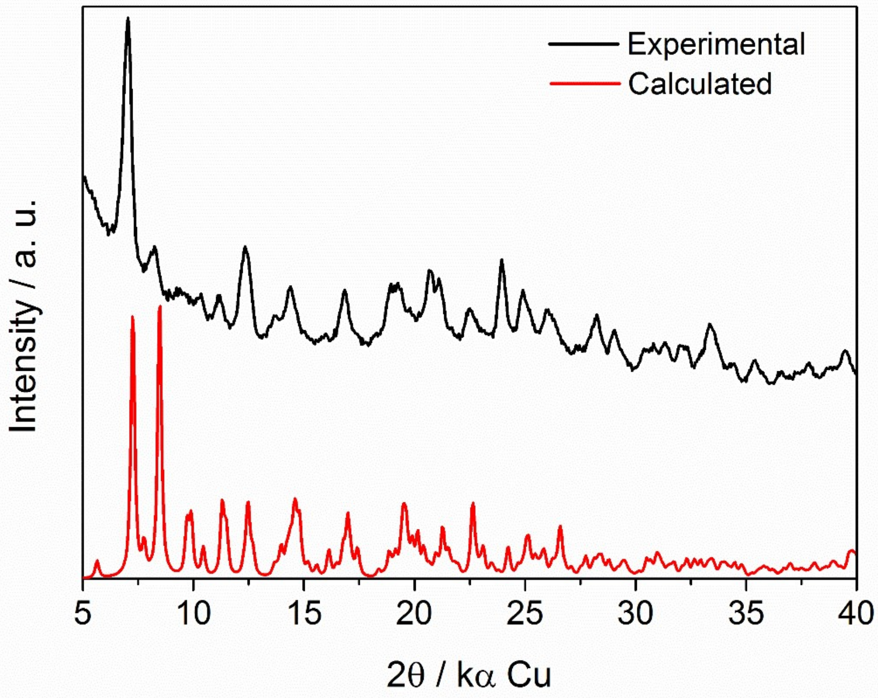

Fig. S16. X-ray diffraction patterns for **1_F**. Experimental (black line): powder diffraction of the bulk. Calculated (red line): simulation from single-crystal employing the Mercury® software.

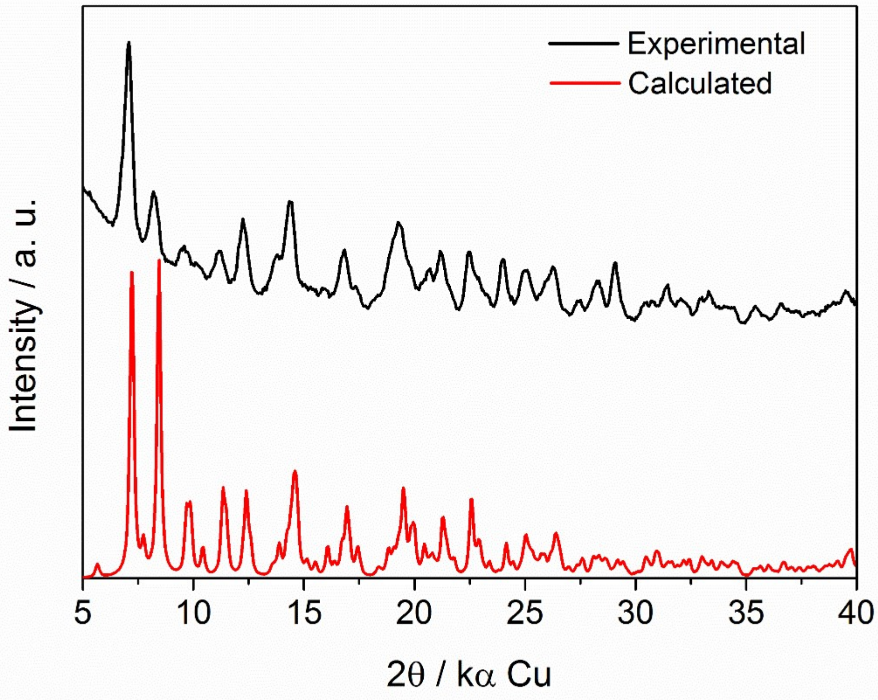

Fig. S17. X-ray diffraction patterns for **2_F**. Experimental (black line): powder diffraction of the bulk. Calculated (red line): simulation from single-crystal results employing the Mercury® software.

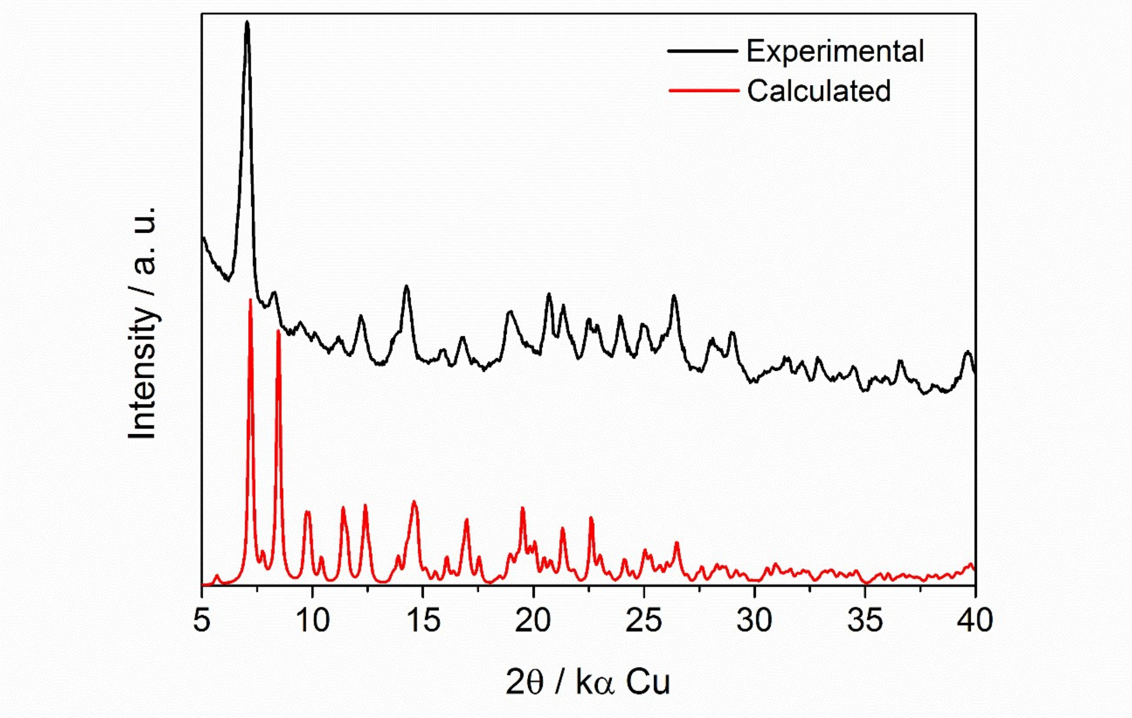

Fig. S18. X-ray diffraction patterns for **3_F**. Experimental (black line): powder diffraction of the bulk. Calculated (red line): simulation from single-crystal results employing the Mercury® software.

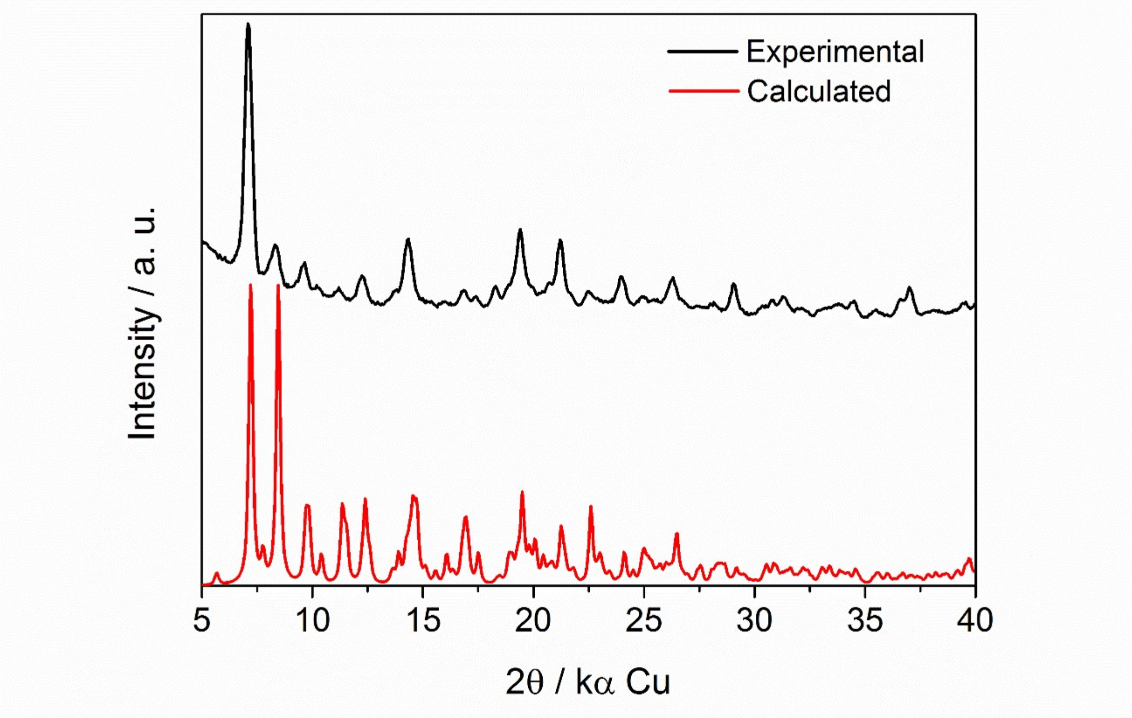

Fig. S19. X-ray diffraction patterns for **4_F**. Experimental (black line): powder diffraction of the bulk. Calculated (red line): simulation from single-crystal results employing the Mercury® software.

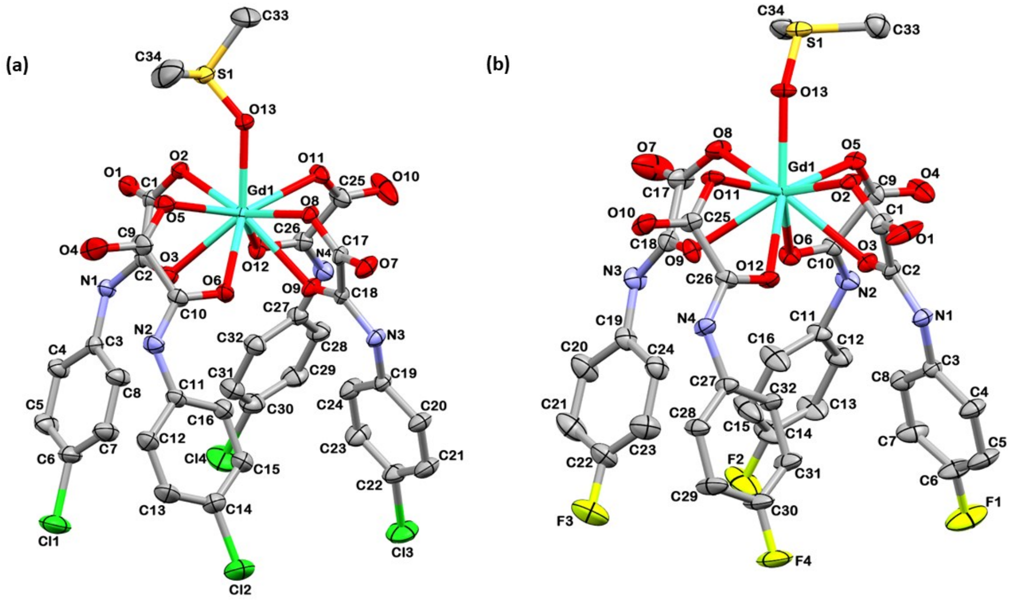

Fig. S20. Crystal structures of (a) **1_Cl** and (b) **1_F** with the atom numbering scheme. Ellipsoids are drawn at 50% probability level. Hydrogen atoms are omitted for the sake of clarity.

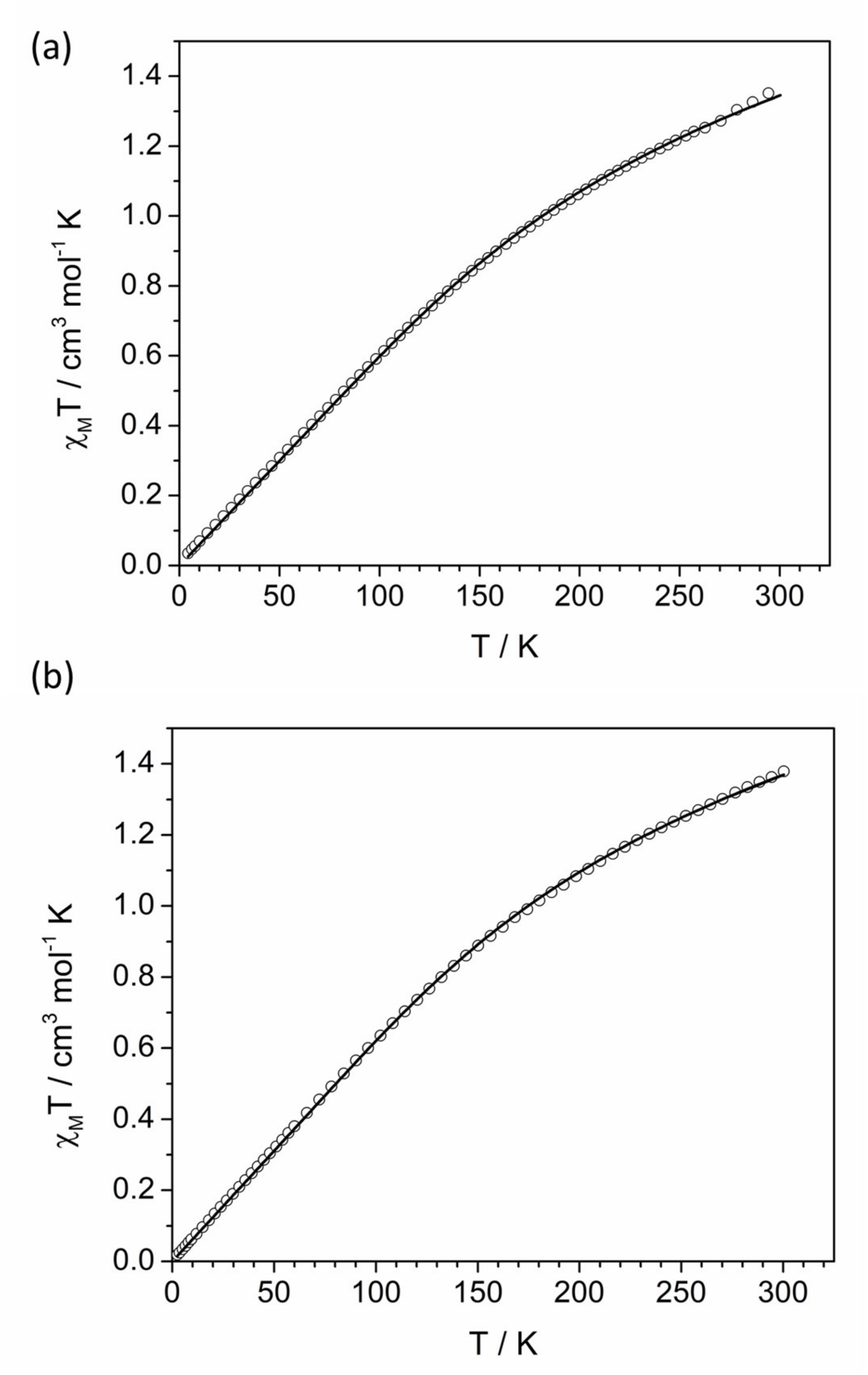

Fig. S21. Temperature dependence of $\chi_M T$ for **1_Cl** (a) and **1_F** (b) under an applied dc field of 1.5 kOe. Solid-lines represent the best-fit curves of the experimental data (o).

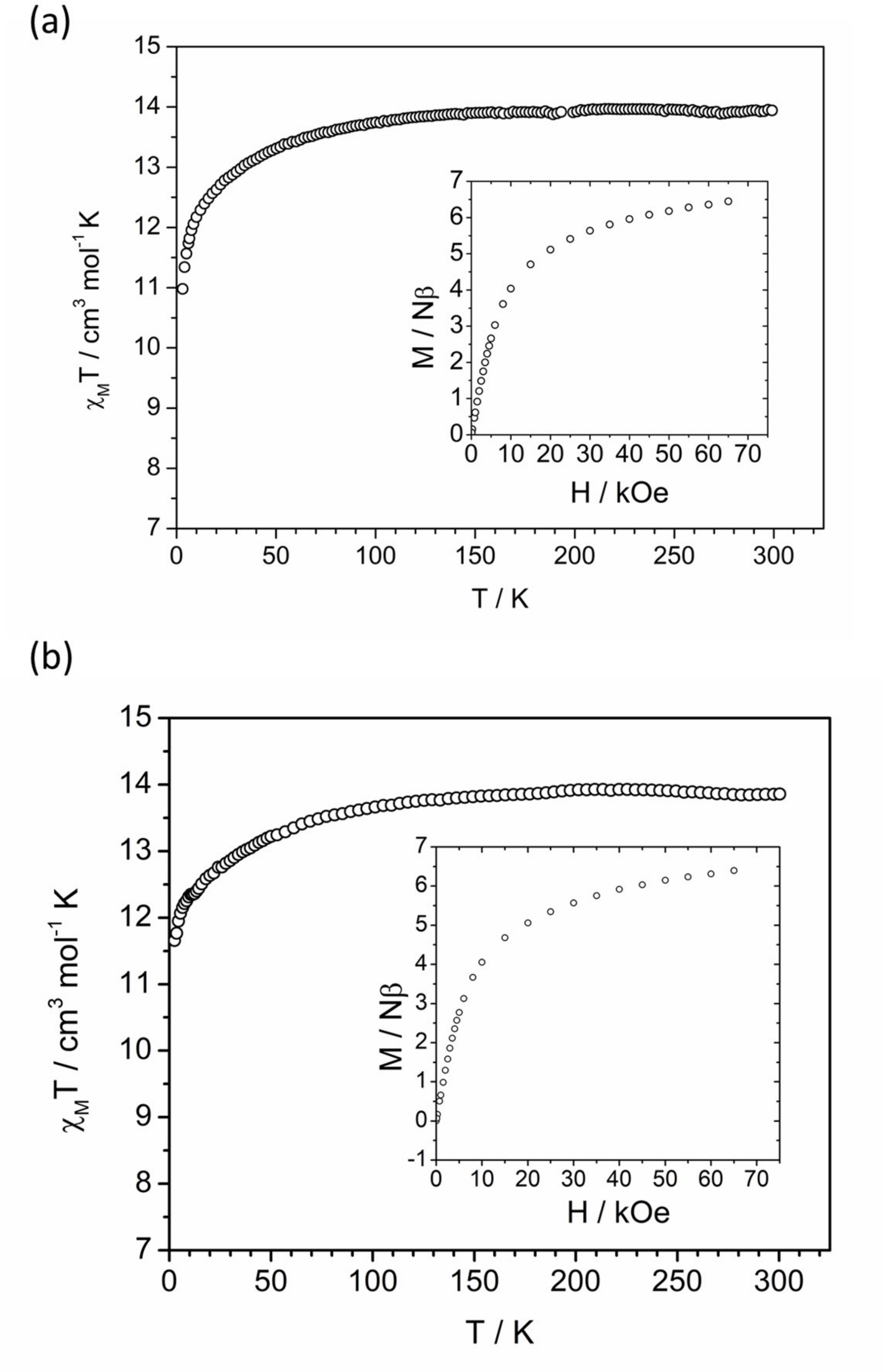

Fig. S22. Temperature dependence of $\chi_M T$ for **3_Cl** (a) and **3_F** (b) under an applied dc field of 200 Oe. The insets show the field dependence of the magnetization (*M*) for **3_Cl** (a) and **3_F** (b) at 3.0 K.

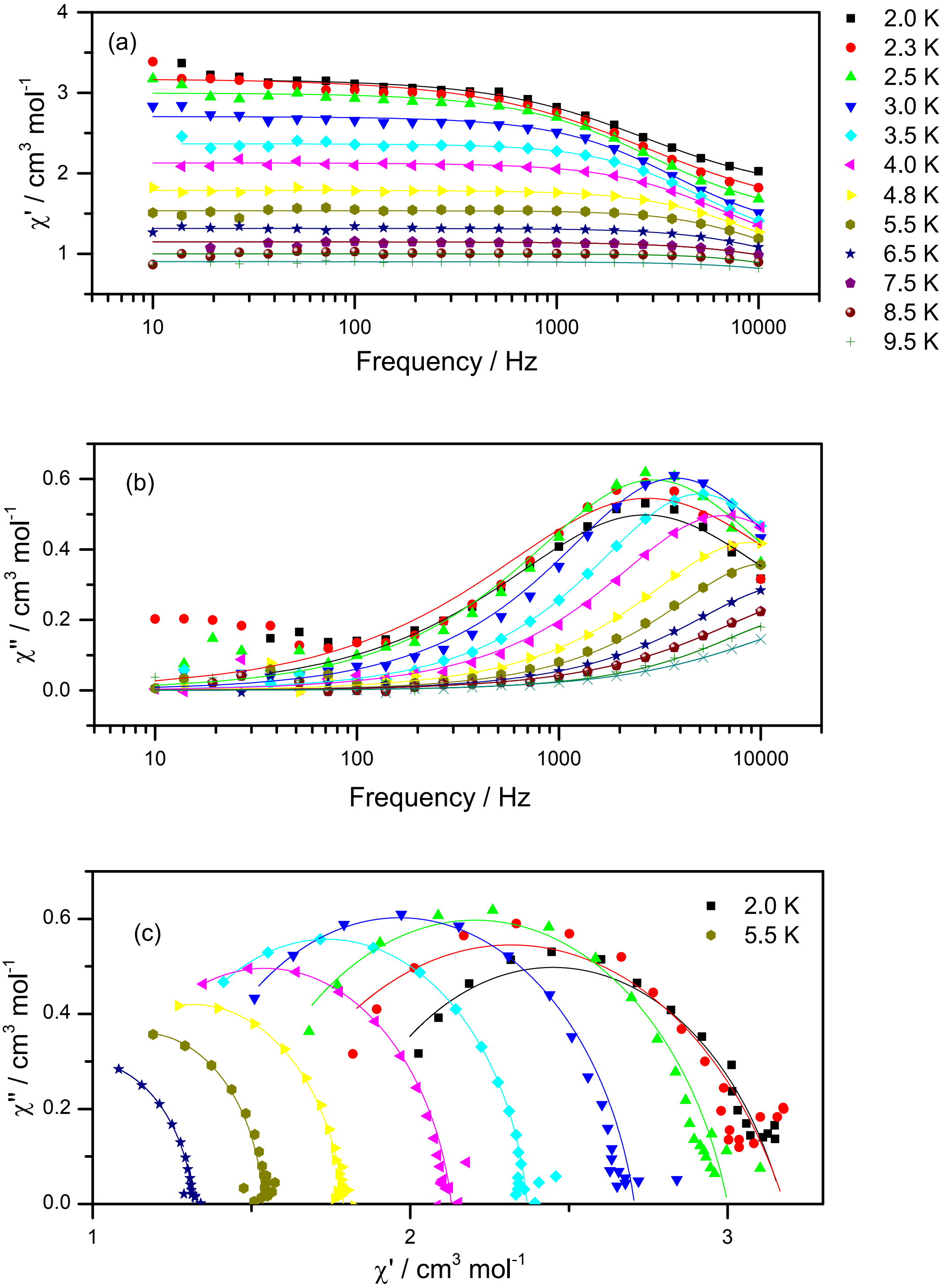

Fig. S23. Ac susceptibility data for **2_Cl** measured under a dc field of 1 kOe: (a, b) frequency dependence of the in-phase and out-of-phase magnetic susceptibility in the temperature range 2.0-5.5 K; (c) Cole-Cole plot for **2_Cl**. The solid lines are the best-fit curves obtained by using a generalized Debye model whose parameters are given in Table S3.

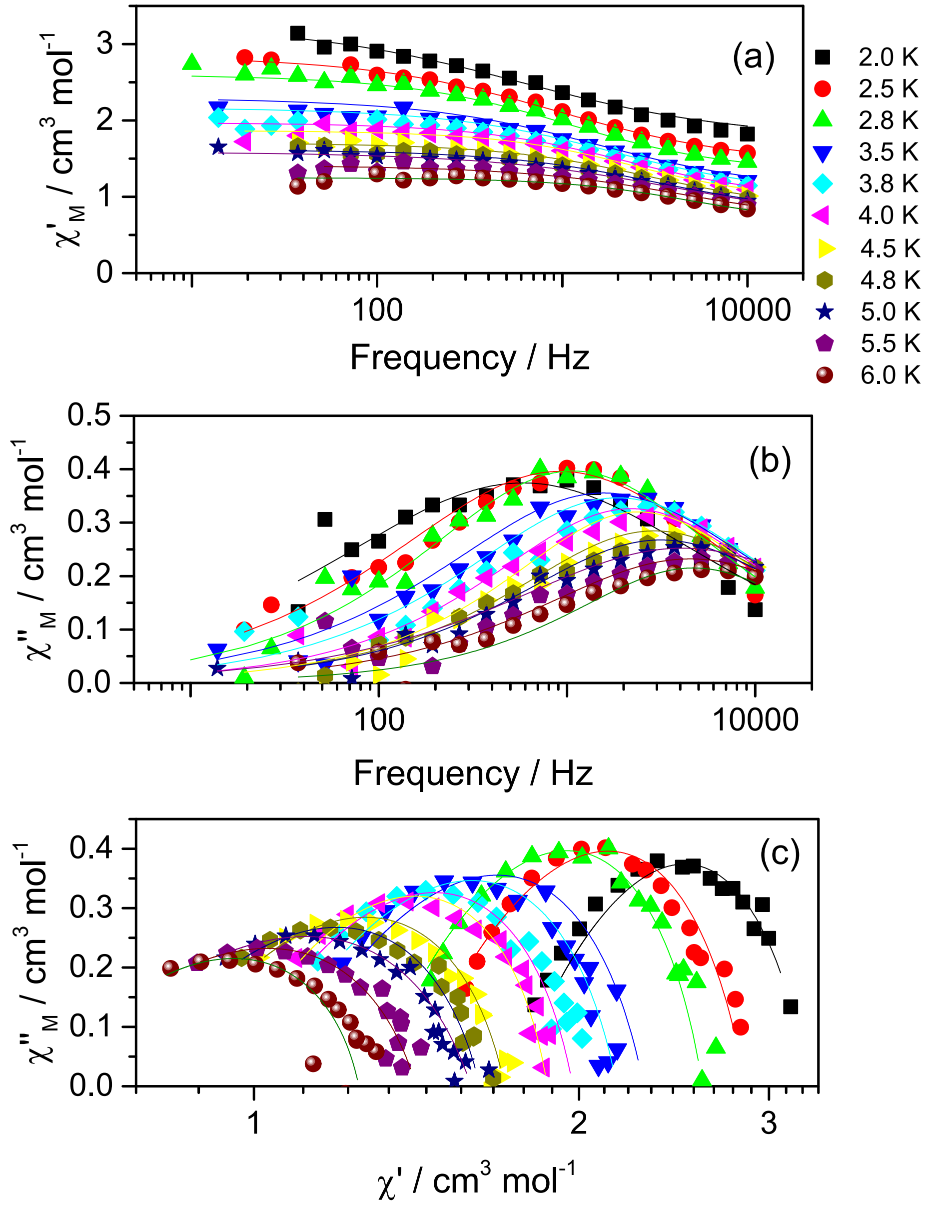

Fig. S24. Ac susceptibility data for **2_F** measured under a dc field of 1 kOe: (a, b) frequency dependence of the in-phase and out-of-phase magnetic susceptibilities in the temperature range 2.0-6.0 K; (c) Cole-Cole plot. The solid lines are the best-fit curves obtained by using a generalized Debye model whose parameters are given in Table S2.

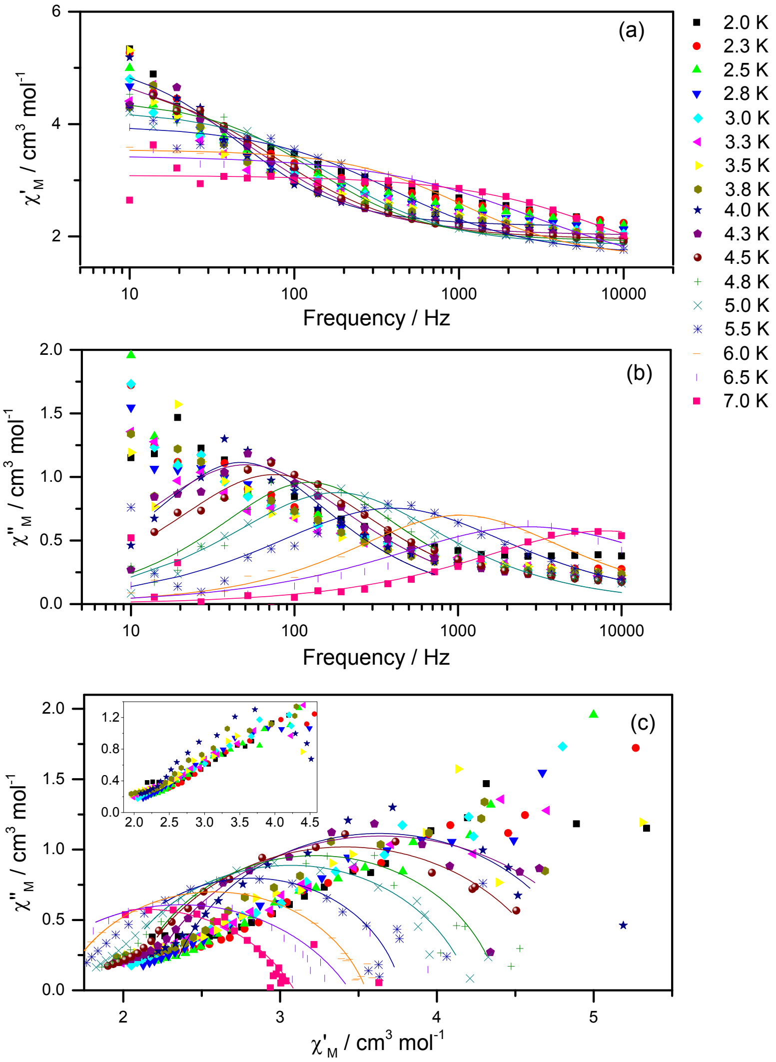

Fig. S25. Ac susceptibility data for **3_Cl** measured under a dc field of 1 kOe: (a, b) frequency dependence of the in-phase and out-of-phase magnetic susceptibility in the temperature range 2.0-7.0 K; (c) Cole-Cole plot of **3_Cl**. The solid lines are the bestfit curves obtained by using a generalized Debye model whose parameters are given in Table S4.

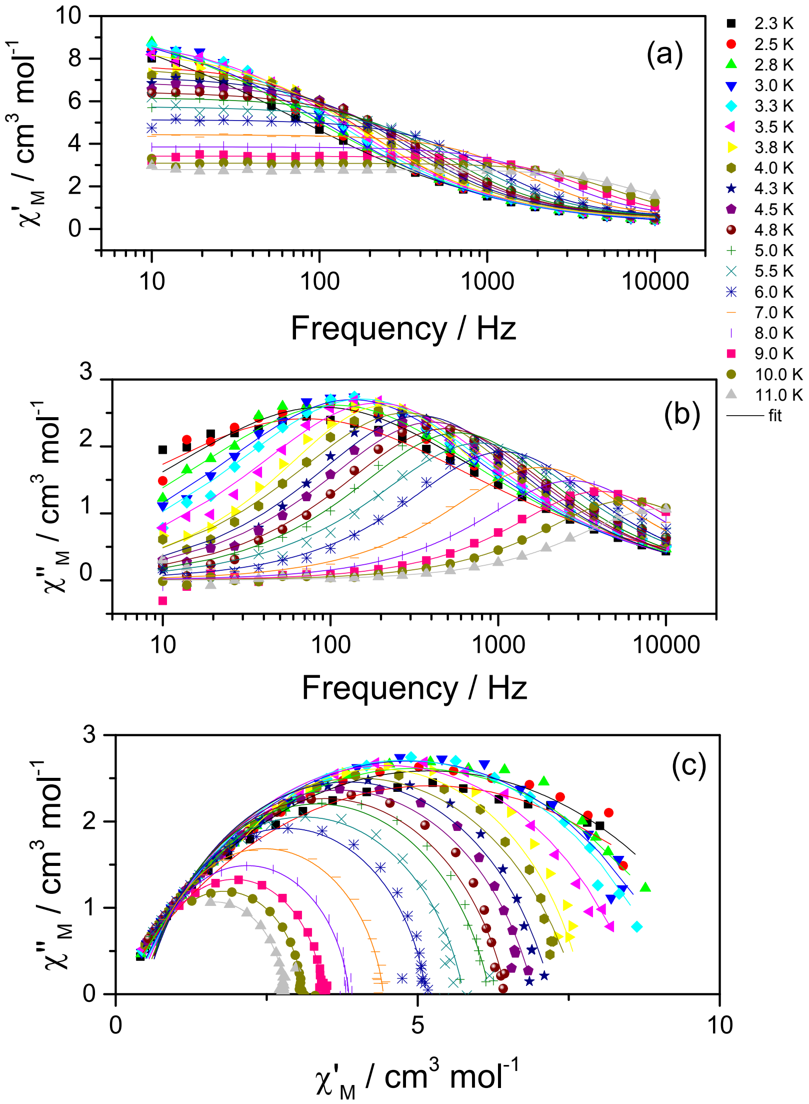

Fig. S26. Ac susceptibility data for **4_F** measured under a dc field of 1 kOe: (a, b) frequency dependence of the in-phase and out-of-phase magnetic susceptibility in the temperature range 2.0-9.0 K; (c) Cole-Cole plot. The solid lines are the best-fit curves obtained by using a generalized Debye model whose parameters are given in Table S5.

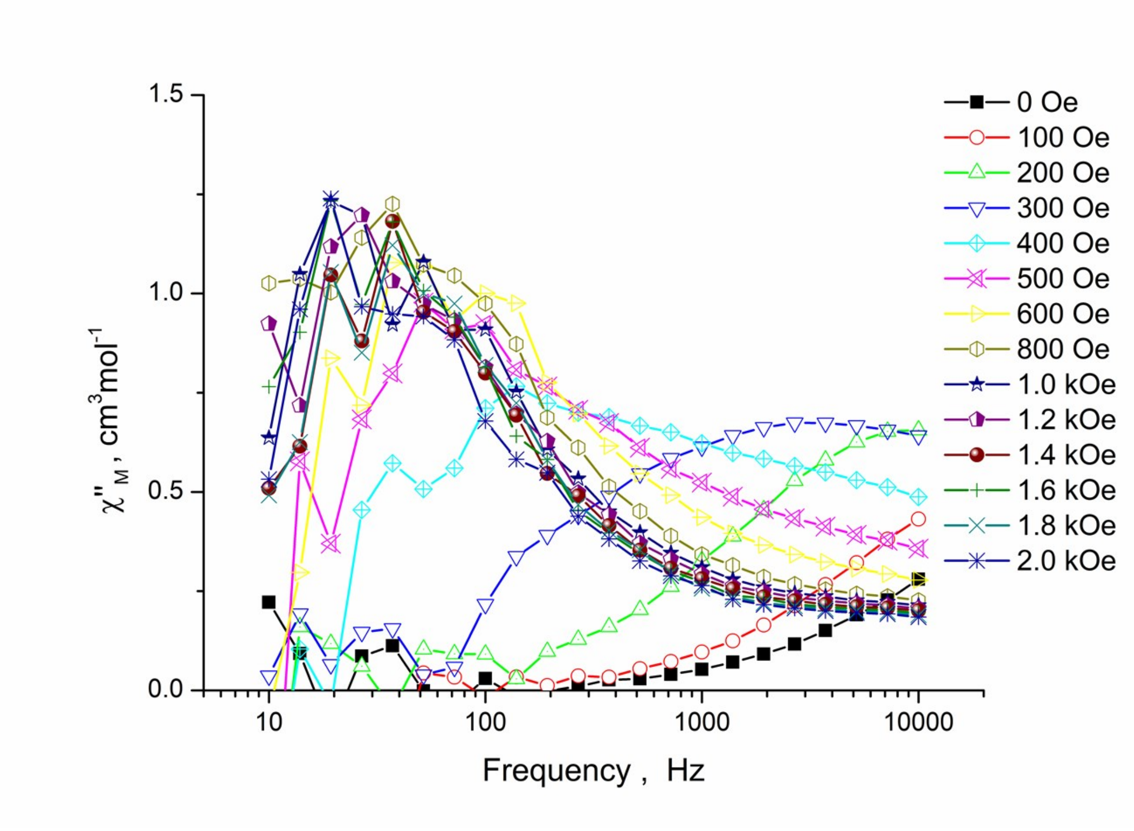

Fig. S27. Frequency dependence of the out-of-phase magnetic susceptibility for **3_Cl** under several applied dc fields at 4.0 K. The solid lines are just eye-guides.

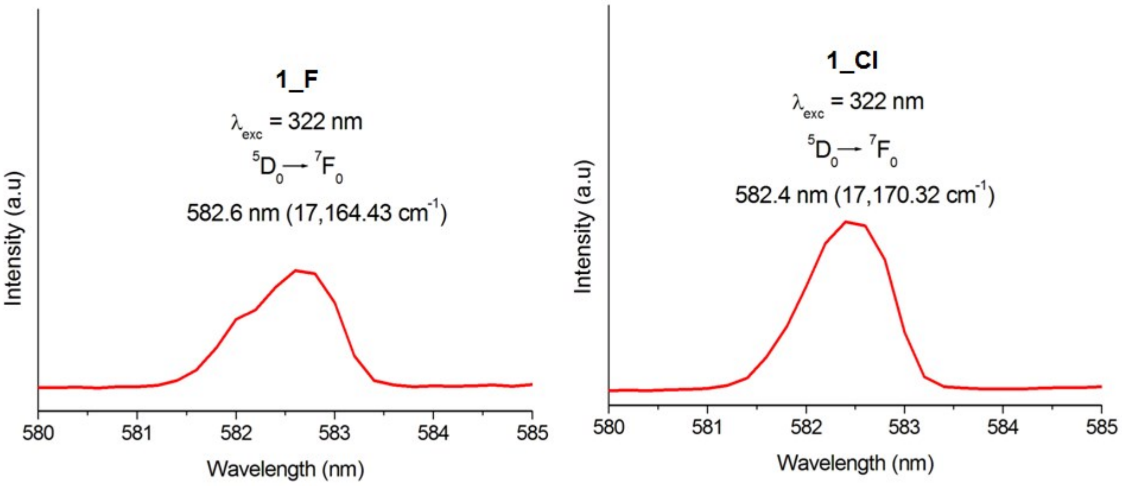

Fig. S28. $^5D_0 \rightarrow {}^7F_0$ transitions for the Eu^{3+} complexes at 77 K.

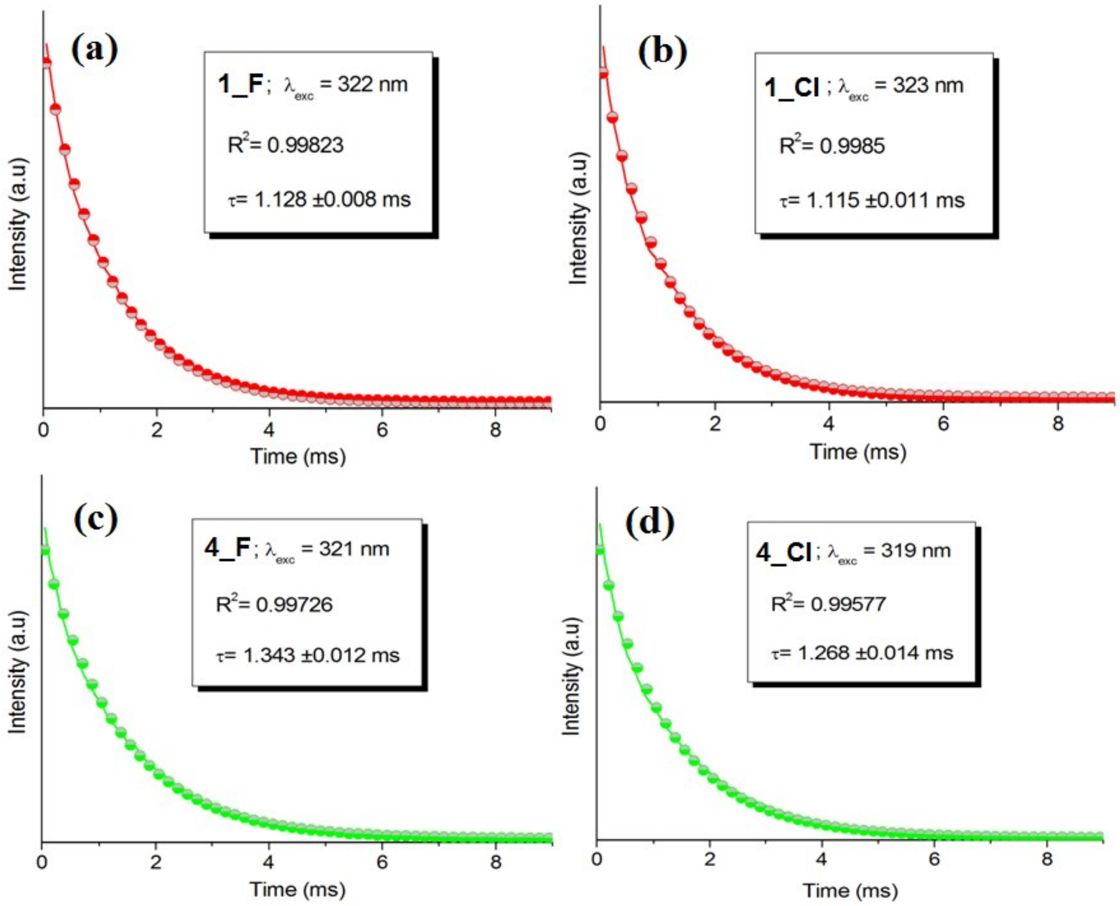

Fig. S29. Lifetimes decays for the Eu^{3+} and Tb^{3+} complexes in the solid-state.

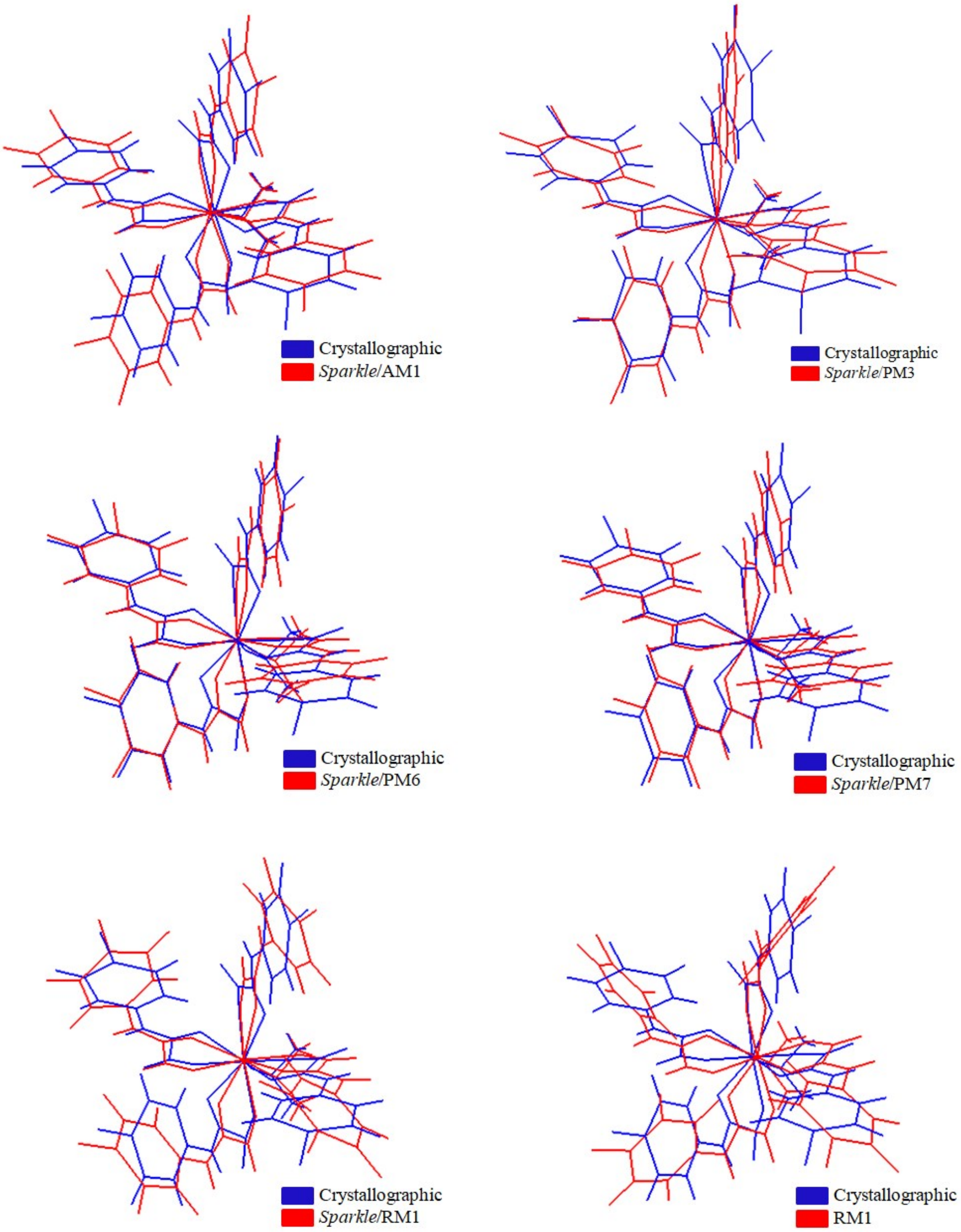

Fig. S30. Overlapping of the calculated structures with the crystal structure for **1_F**.

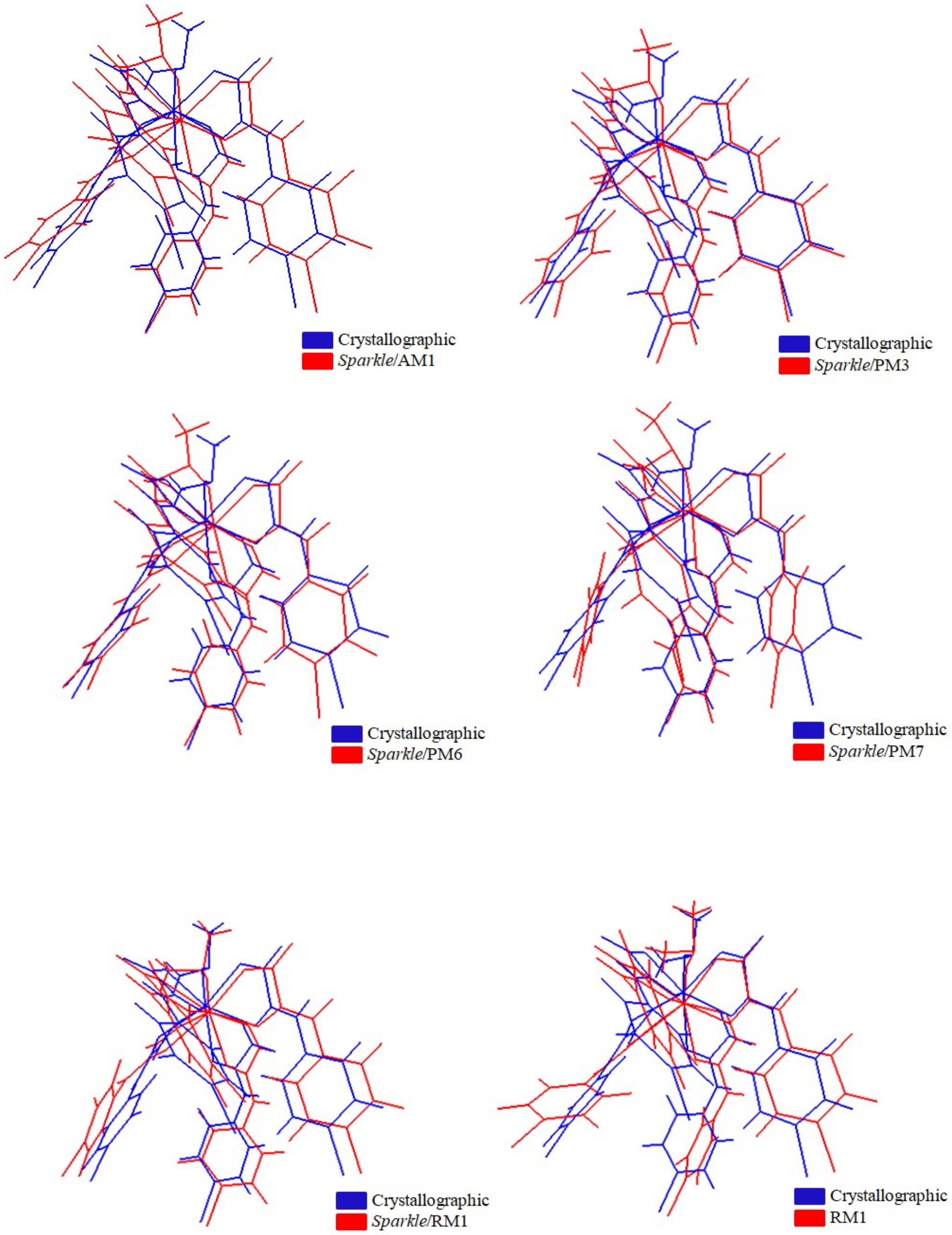

Fig. S31. Overlapping of the calculated structures with the crystal structure for **1_Cl**.

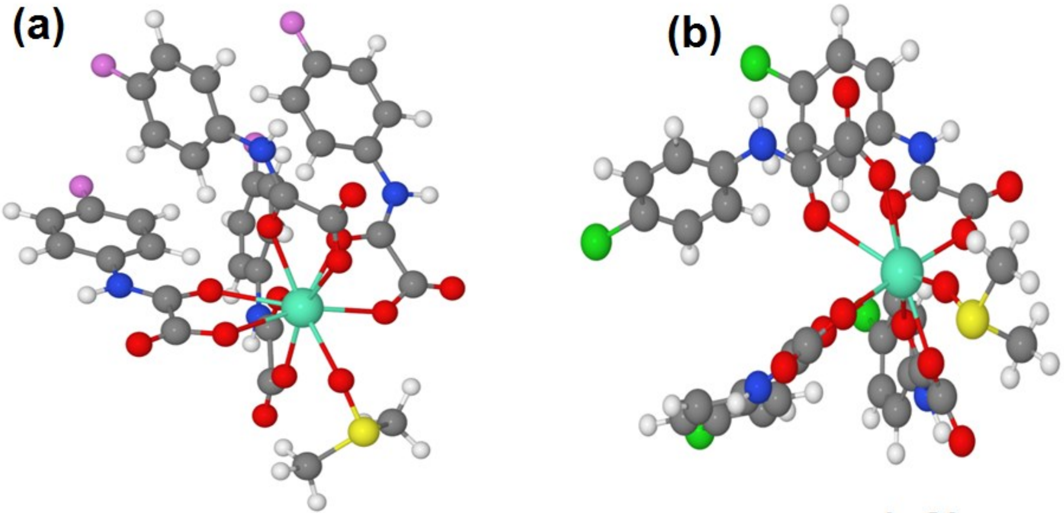

1_F
(Sparkle/PM6)

1_Cl
(Sparkle/RM1)

Fig. S32. Ground state geometry for **1_F** and **1_Cl** calculated by the Sparkle/PM6 and Sparkle/RM1 models. Color codes: C, light-gray; H, white; O, red; N, blue; F, pink; Cl, green; S, yellow and Eu, light-green.

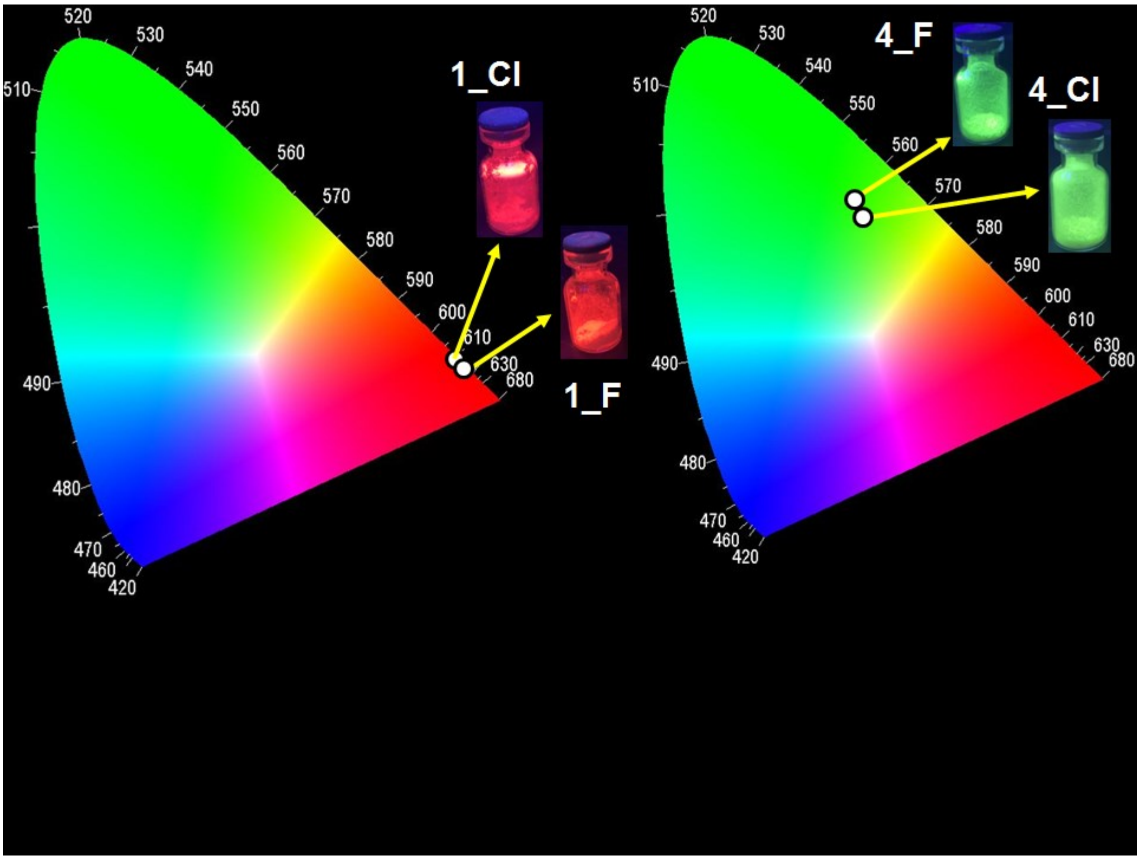

Fig. S33. CIE diagram obtained from the emission spectra of t**1_F**, **1_Cl**, **4_F** and **4_Cl** with photographs illustrating their intense red-orange and green photoluminescences under UV irradiation.

Table S1. Experimental and calculated $\chi_M T$ values at room temperature for **1_Cl**, **1_F**, **2_Cl, 2_F, 3_Cl, 3_F, 4_Cl, 4_F**.

Compound	**Theory**				**Calculated*** $\chi_M T$ **(cm^3 K mol^{-1})**	**Experimental** $\chi_M T$ **(cm^3 K mol^{-1})**
	g_J	*S*	*L*	Free ion term		
1_Cl	5	6/2	3	$^7F_0$	0	1.37
1_F	5	6/2	3	$^7F_0$	0	1.37
2_Cl	2	7/2	0	$^8S_{7/2}$	7.88	7.66
2_F	2	7/2	0	$^8S_{7/2}$	7.88	7.71
3_Cl	4/3	5/2	5	$^6H_{15/2}$	14.17	13.94
3_F	4/3	5/2	5	$^6H_{15/2}$	14.17	13.85
4_Cl	3/2	3	3	$^7F_6$	11.82	10.90
4_F	3/2	3	3	$^7F_6$	11.82	11.10

* Estimated values are obtained by using the expression of the free ion. g_J = Landé factor *g* of *J* state; *S* = spin of the ion; *L* = orbital momentum; χ_M = molar magnetic susceptibility; *T* = temperature.

Table S2. Best-fit parameters of the generalized Debye model for **2_F** measured under a dc field of 1 kOe. ErrUp and ErrDown are uncertainties of τ calculated considering the contribution of the α parameter of the Generalized Debye model.

T/K	χ_s/cm^3 Kmol^{-1}	χ_T/cm^3 K/mol^{-1}	α	τ/s	ErrUp (s)	ErrDown (s)
2.00	1.74(4)	3.27(4)	0.42(3)	2.7(2)x10^{-4}	0.00179	2.3 x10^{-4}
2.50	1.40(3)	2.85(2)	0.36(2)	1.73(9)x10^{-4}	7.8 x10^{-4}	1.4 x10^{-4}
2.75	1.29(5)	2.60(3)	0.30(3)	1.48(15)x10^{-4}	4.7 x10^{-4}	1.1 x10^{-4}
3.25	1.08(4)	2.33(2)	0.34(3)	1.02(8)x10^{-4}	4.1 x10^{-4}	8.2 x10^{-5}
3.50	1.01(4)	2.169(18)	0.31(3)	8.6(8)x10^{-5}	2.9 x10^{-4}	6.6 x10^{-5}
3.75	0.96(5)	1.97(2)	0.27(4)	7.3(8)x10^{-5}	1.9 x10^{-4}	5.3 x10^{-5}
4.00	0.95(5)	1.87(2)	0.22(4)	6.7(8)x10^{-5}	1.3 x10^{-4}	4.4 x10^{-5}
4.50	0.83(4)	1.707(13)	0.27(3)	5.5(5)x10^{-5}	1.4 x10^{-4}	3.9 x10^{-5}
4.75	0.77(5)	1.636(14)	0.28(4)	5.0(6)x10^{-5}	1.4x10^{-4}	3.7 x10^{-5}
5.00	0.65(6)	1.589(13)	0.37(3)	3.9(6)x10^{-5}	1.9 x10^{-4}	3.2 x10^{-5}
5.50	0.65(6)	1.414(15)	0.31(5)	3.5(6)x10^{-6}	1.2 x10^{-4}	2.7 x10^{-5}
6.00	0.66(6)	1.251(14)	0.19(7)	3.4(6)x10^{-6}	5.6 x10^{-5}	2.1 x10^{-5}
6.50	0.60(4)	1.192(8)	0.25(4)	3.1(4)x10^{-6}	7.3 x10^{-5}	2.2 x10^{-5}

Table S3. Best-fit parameters of the generalized Debye model for **2_Cl** measured under a dc field of 1 kOe. ErrUp and ErrDown are uncertainties of τ calculated considering the contribution of the α parameter of the Generalized Debye model.

T/K	χ_s/cm^3 Kmol^{-1}	χ_T/cm^3 K/mol^{-1}	α	τ/s	ErrUp (s)	ErrDown (s)
2.00	1.73(5)	3.172(16)	0.23(3)	5.9(4)x10^{-5}	1.2 x10^{-4}	4.0 x10^{-5}
2.25	1.46(12)	3.18(3)	0.28(6)	5.8(9)x10^{-5}	1.6 x10^{-5}	4.3 x10^{-5}
2.50	1.41(8)	3.00(2)	0.18(4)	5.4(5)x10^{-5}	8.4 x10^{-5}	3.3 x10^{-5}
3.00	1.23(4)	2.71(2)	0.13(2)	4.2(2)x10^{-5}	4.7 x10^{-5}	2.2 x10^{-5}
3.50	1.11(4)	2.368(8)	0.08(2)	3.20(15)x10^{-5}	2.4 x10^{-5}	1.4 x10^{-5}
4.00	0.96(7)	2.129(9)	0.11(3)	2.4(2)x10^{-5}	2.3 x10^{-5}	1.2 x10^{-5}
4.75	0.84(5)	1.789(5)	0.08(3)	1.80(15)x1^{-5}	1.3 x10^{-5}	7.7 x10^{-6}
5.50	0.78(11)	1.536(8)	0.03(6)	1.5(3)x10^{-5}	5.8 x10^{-6}	4.2 x10^{-6}

Table S4. Best-fit parameters of the generalized Debye model for **3_Cl** measured under a dc field of 1 kOe. ErrUp and ErrDown are uncertainties of τ calculated considering the contribution of the α parameter of the Generalized Debye model.

T/K	χ_s/cm^3 Kmol^{-1}	χ_T/cm^3 K mol^{-1}	α	τ/s	ErrUp (s)	ErrDown (s)
4.00	2.28(4)	4.99(8)	0.12(3)	3.4(2)x10^{-3}	0.00356	0.00174
4.25	2.11(5)	5.17(10)	0.20(3)	3.2(2)x10^{-3}	0.00565	0.00204
4.50	2.03(4)	4.79(5)	0.19(2)	2.1(2)x10^{-3}	0.00354	0.00133
4.75	2.05(9)	4.39(7)	0.13(4)	1.3(2)x10^{-3}	0.00146	6.9 x10^{-4}
5.00	1.88(4)	4.23(4)	0.18(2)	9(4)x10^{-4}	0.00138	5.4 x10^{-4}
5.50	1.86(5)	3.77(3)	0.12(4)	4(3)x10^{-4}	4.2 x10^{-4}	2.0 x10^{-4}
6.00	1.60(3)	3.550(14)	0.207(15)	1.54(5)x10^{-4}	2.8 x10^{-4}	9.9 x10^{-5}
6.50	1.3(3)	3.44(6)	0.5(8)	5.8(17)x10^{-5}	7.0 x10^{-4}	5.4 x10^{-5}
7.00	1.2(6)	3.09(6)	0.31(12)	1.9(13)x10^{-5}	6.4 x10^{-5}	1.5 x10^{-5}

Table S5. Best-fit parameters of the generalized Debye model for **4_F** measured under a dc field of 2 kOe. ErrUp and ErrDown are uncertainties of τ calculated considering the contribution of the α parameter of the Generalized Debye model.

T/K	χ_s/cm^3 Kmol^{-1}	χ_T/cm^3 K mol^{-1}	α	τ/s	ErrUp (s)	ErrDown (s)
2.25	0.00(5)	10.45(13)	0.449(8)	2.23(5)x10^{-3}	0.01817	0.00199
2.50	0.00(15)	10.38(15)	0.412(15)	1.78(7)x10^{-3}	0.0112	0.00154
2.75	0.13(4)	9.95(8)	0.367(7)	1.46(3)x10^{-3}	0.00687	0.0012
3.00	0.24(5)	9.44(9)	0.324(10)	1.18(3)x10^{-3}	0.00428	9.2 x10^{-4}
3.25	0.28(5)	9.23(7)	0.307(8)	1.04(2)x10^{-3}	0.00342	7.9 x10^{-4}
3.50	0.34(5)	8.65(7)	0.278(10)	8.4(2)x10^{-4}	0.00233	6.2 x10^{-4}
3.75	0.98(13)	7.84(6)	0.164(18)	7.7(3)x10^{-4}	0.00109	4.5 x10^{-4}
4.00	0.42(6)	7.63(6)	0.228(13)	5.63(15)x10^{-4}	0.00117	3.8 x10^{-4}
4.25	0.48(7)	7.21(6)	0.197(15)	4.65(14)x10^{-4}	8.1 x10^{-4}	2.9 x10^{-4}
4.50	0.45(6)	6.92(5)	0.196(12)	3.96(10)x10^{-4}	6.8 x10^{-4}	2.5 x10^{-4}
4.75	0.48(6)	6.53(5)	0.176(13)	3.3(8)x10^{-4}	5.0 x10^{-4}	2.0 x10^{-4}
5.00	0.48(6)	6.19(4)	0.163(15)	2.7(8)x10^{-4}	3.8 x10^{-4}	1.6 x10^{-4}
5.50	0.46(8)	5.76(5)	0.162(18)	2.05(7)x10^{-4}	2.9 x10^{-4}	1.2 x10^{-4}
6.00	0.50(6)	5.14(3)	0.119(15)	1.48(4)x10^{-4}	1.5 x10^{-4}	7.5 x10^{-5}
7.00	0.49(4)	4.431(17)	0.099(11)	8.96(18)x10^{-5}	8.0 x10^{-5}	4.2 x10^{-5}
8.00	0.50(4)	3.858(13)	0.077(11)	5.82(12)x10^{-5}	4.2 x10^{-5}	2.4 x10^{-5}
9.00	0.51(9)	3.42(2)	0.06(2)	3.97(17)x10^{-5}	2.4 x10^{-5}	1.5 x10^{-5}
10.00	0.50(8)	3.092(13)	0.05(2)	2.71(12)x10^{-5}	1.4 x10^{-5}	9.4 x10^{-6}
11.00	0.50(19)	2.789(18)	0.04(4)	1.7(2)x10^{-5}	7.8 x10^{-6}	5.4 x10^{-6}

Table S6. Best-fit parameters of the generalized Debye model for **4_Cl** measured under a DC field of 2 kOe. ErrUp and ErrDown are uncertainties of τ calculated considering the contribution of the α parameter of the Generalized Debye model.

T/K	χ_s/cm^3 K mol^{-1}	χ_T/cm^3 K mol^{-1}	α	τ/s	ErrUp (s)	ErrDown (s)
2.25	0.01(2)	3.36(2)	0.393(7)	1.72(3)x10^{-4}	9.5 x10^{-4}	1.4 x10^{-4}
2.50	0.04(3)	3.68(3)	0.371(9)	1.84(4)x10^{-4}	8.9 x10^{-4}	1.5 x10^{-4}
3.00	0.05(8)	4.04(4)	0.342(19)	1.77(9)x10^{-4}	7.2 x10^{-4}	1.4 x10^{-4}
3.25	0.13(8)	3.99(4)	0.308(19)	1.67(9)x10^{-4}	5.5 x10^{-4}	1.3 x10^{-4}
3.50	0.27(6)	3.84(3)	0.241(17)	1.57(6)x10^{-4}	3.5 x10^{-4}	1.1 x10^{-4}
3.75	0.28(4)	3.78(2)	0.233(12)	1.50(4)x10^{-4}	3.2 x10^{-4}	1.0 x10^{-4}
4.00	0.29(5)	3.68(2)	0.227(14)	1.40(4)x10^{-4}	2.9 x10^{-4}	9.4 x10^{-4}
4.25	0.32(5)	3.51(2)	0.206(15)	1.28(4)x10^{-4}	2.3 x10^{-4}	8.3 x10^{-5}
4.50	0.33(4)	3.39(2)	0.195(14)	1.19(4)x10^{-4}	2.0 x10^{-4}	7.5 x10^{-5}
4.75	0.32(3)	3.280(13)	0.195(9)	1.11(2)x10^{-4}	1.9 x10^{-4}	7.0 x10^{-5}
5.00	0.36(4)	3.096(19)	0.166(16)	1.01(3)x10^{-4}	1.4 x10^{-4}	5.9 x10^{-5}
5.50	0.37(4)	2.843(14)	0.141(15)	0.80(2)x10^{-4}	9.7 x10^{-5}	4.4 x10^{-5}
6.00	0.37(6)	2.67(2)	0.14(2)	0.71(3)x10^{-4}	8.6 x10^{-5}	3.9 x10^{-5}
6.50	0.32(6)	2.517(16)	0.15(2)	0.57(3)x10^{-4}	7.4 x10^{-5}	3.2 x10^{-5}
7.00	0.36(4)	2.316(11)	0.112(18)	0.473(18)x10^{-4}	4.7 x10^{-5}	2.3 x10^{-5}

Table S7. Calculated values of the intramolecular energy transfer and back-transfer rates for **1_F** and **1_Cl**.

System	Energy Transfer Rates (s^{-1})		Energy Back-Transfer Rates (s^{-1})	
1_F	$S_1 \rightarrow {}^5D_4$	4.38 x 10^{-1}	$S_1 \leftarrow {}^5D_4$	4.26 x 10^{-26}
	$T_1 \rightarrow {}^5D_4$	1.53 x 10^{3}	$T_1 \leftarrow {}^5D_4$	1.81 x 10^{0}
	$T_1 \rightarrow {}^5G_6$	3.22 x 10^{1}	$T_1 \leftarrow {}^5G_6$	6.98 x 10^{-4}
	$T_1 \rightarrow {}^5L_6$	7.65 x 10^{1}	$T_1 \leftarrow {}^5L_6$	1.77 x 10^{-6}
	$T_1 \rightarrow {}^5D_1$	3.52 x 10^{6}	$T_1 \leftarrow {}^5D_1$	6.20x 10^{-15}
	$T_1 \rightarrow {}^5D_0$	5.74 x 10^{5}	$T_1 \leftarrow {}^5D_0$	2.48x 10^{-19}
1_Cl	$S_1 \rightarrow {}^5D_4$	2.93 x 10^{-1}	$S_1 \leftarrow {}^5D_4$	6.95 x 10^{-27}
	$T_1 \rightarrow {}^5D_4$	1.77 x 10^{3}	$T_1 \leftarrow {}^5D_4$	3.57 x 10^{2}
	$T_1 \rightarrow {}^5G_6$	4.14 x 10^{1}	$T_1 \leftarrow {}^5G_6$	1.54 x 10^{-1}
	$T_1 \rightarrow {}^5L_6$	1.20 x 10^{2}	$T_1 \leftarrow {}^5L_6$	4.76 x 10^{-4}
	$T_1 \rightarrow {}^5D_1$	1.33 x 10^{7}	$T_1 \leftarrow {}^5D_1$	4.02 x 10^{-12}
	$T_1 \rightarrow {}^5D_0$	2.78 x 10^{6}	$T_1 \leftarrow {}^5D_0$	2.05 x 10^{-16}

Table S8. RMSD values obtained by overlapping the crystal structure with the calculated structures of **1_F**. The RMSD calculations were carried out considering that each pair of molecules has different orientations, so rotations were applied in order to minimize the RMSD value.

Method	RMSD (Å)
Crystallographic	0.000
Sparkle/AM1	0.570
Sparkle/PM3	0.508
Sparkle/PM6	**0.485**
Sparkle/PM7	0.527
Sparkle/RM1	0.748
RM1	0.974

Table S9. RMSD values obtained by overlapping the crystal structure with the calculated structures of **1_Cl**. The RMSD calculations were carried out considering that each pair of molecules has different orientations, so rotations were applied in order to minimize the RMSD value.

Method	RMSD (Å)
Crystallographic	0.000
Sparkle/AM1	0.967
Sparkle/PM3	0.899
Sparkle/PM6	0.939
Sparkle/PM7	1.223
Sparkle/RM1	**0.831**
RM1	1.005

Table S10. Spherical atomic coordinates for the Sparkle/PM6 coordination polyhedron with charge factor (*g*) and polarizability (α) of the coordinated atoms in **1_F**.

Atom	*R* (Å)	Θ (°)	Φ (°)	*g*	α (Å^3)
Eu	0.0000	0.00	0.00	---	---
O	2.4478	40.59	174.68	0.0117	4.0617
O	2.4641	85.66	134.05	0.0115	4.0640
O	2.4467	51.47	4.28	0.0117	4.0723
O	2.4626	66.65	69.34	0.0115	4.0723
O	2.4531	134.83	323.63	0.0117	4.0614
O	2.4635	124.27	38.57	0.0115	4.0606
O	2.4541	123.61	209.93	0.0117	4.0613
O	2.4660	147.50	130.40	0.0115	4.0644
O	2.3985	78.91	267.63	0.0120	4.0626

Table S11. Spherical atomic coordinates for the Sparkle/RM1 coordination polyhedron with charge factor (g) and polarizability (α) of the coordinated atoms in **1_Cl**.

Atom	*R* (Å)	Θ (°)	Φ (°)	*g*	α (Å^3)
Eu	0.0000	0.00	0.00	---	---
O	2.4782	36.27	19.88	0.0106	3.7457
O	2.5168	69.85	318.87	0.0104	3.7526
O	2.4833	126.91	10.86	0.0106	3.7433
O	2.5181	133.63	293.95	0.0104	3.7455
O	2.4888	142.71	149.27	0.0106	3.7486
O	2.5220	112.13	213.19	0.0103	3.7475
O	2.4810	57.39	162.02	0.0106	3.7442
O	2.5178	44.49	236.16	0.0104	3.7473
O	2.4133	99.40	87.22	0.0111	3.7458

References

1 F. R. Fortea-Pérez, F. Neve, D. Armentano, G. De Munno, S.-E. E. Stiriba and M. Julve, *Inorganica Chim. Acta*, 2016, **443**, 267–273.

2 F. R. Fortea-Pérez, B. L. Rothenpieler, N. Marino, D. Armentano, G. De Munno, M. Julve and S.-E. Stiriba, *Inorg. Chem. Front.*, 2015, **2**, 1029–1039.

3 T. T. da Cunha, V. M. M. Barbosa, W. X. C. Oliveira, C. B. Pinheiro, E. F. Pedroso, W. C. Nunes and C. L. M. Pereira, *Polyhedron*, 2019, **169**, 102–113.

4 W. D. Do Pim, T. R. G. Simões, W. X. C. Oliveira, I. R. A. Fernandes, C. B. Pinheiro, F. Lloret, M. Julve, H. O. Stumpf and C. L. M. Pereira, *Cryst. Growth Des.*, 2014, **14**, 5929–5937.

5 G. A. Bain and J. F. Berry, *J. Chem. Educ.*, 2008, **85**, 532.

6 U. APEX2; Bruker AXS Inc, Madison, Wisconsin, 2009.

7 E. CrysAlisPRO. Rigaku Oxford Diffraction: Yarnton, Oxfordshire, 2018.

8 L. Krause, R. Herbst-Irmer, G. M. Sheldrick and D. Stalke, *J. Appl. Crystallogr.*, 2015, **48**, 3–10.

9 G. M. Sheldrick, *Acta Crystallogr. Sect. C Struct. Chem.*, 2015, **71**, 3–8.

10 L. Palatinus and G. Chapuis, *J. Appl. Crystallogr.*, 2007, **40**, 786–790.

11 L. J. Farrugia, *J. Appl. Crystallogr.*, 1999, **32**, 837–838.

12 C. F. Macrae, I. J. Bruno, J. A. Chisholm, P. R. Edgington, P. McCabe, E. Pidcock, L. Rodriguez-Monge, R. Taylor, J. Van De Streek and P. A. Wood, *J. Appl. Crystallogr.*, 2008, **41**, 466–470.

13 L. J. Farrugia, *J. Appl. Crystallogr.*, 1997, 30, 565.

14 W. T. Carnall, H. Crosswhite and H. M. Crosswhite, *Energy level structure and transition probabilities in the spectra of the trivalent lanthanides in* LaF_3, Argonne, IL (United States), 1978.

15 K. Dolgaleva and R. W. Boyd, *Adv. Opt. Photonics*, 2012, **4**, 1.

16 R. O. Freire, R. Q. Albuquerque, S. A. Junior, G. B. Rocha and M. E. De Mesquita, *Chem. Phys. Lett.*, 2005, **405**, 123–126.

17 L. D. Carlos, R. A. S. Ferreira, V. de Z. Bermudez and S. J. L. Ribeiro, *Adv. Mater.*, 2009, **21**, 509–534.

18 M. Dolg, H. Stoll and H. Preuss, *J. Chem. Phys.*, 1989, **90**, 1730–1734.

19 G. B. Rocha, R. O. Freire, A. M. Simas and J. J. P. Stewart, *J. Comput. Chem.*, 2006, **27**, 1101–1111.

20 R. O. Freire, G. B. Rocha and A. M. Simas, *Chem. Phys. Lett.*, 2006, **425**, 138–141.

21 R. O. Freire, N. B. Da Costa, G. B. Rocha and A. M. Simas, *J. Chem. Theory Comput.*, 2006, **2**, 64–74.

22 R. O. Freire, G. B. Rocha and A. M. Simas, *Inorg. Chem.*, 2005, **44**, 3299–3310.

23 R. O. Freire, G. B. Rocha and A. M. Simas, *J. Mol. Model.*, 2006, **12**, 373–389.

24 R. O. Freire, G. B. Rocha and A. M. Simas, *J. Braz. Chem. Soc.*, 2009, **20**, 1638–1645.

25 R. O. Freire and A. M. Simas, *J. Chem. Theory Comput.*, 2010, **6**, 2019–2023.

26 J. D. L. Dutra, M. A. M. Filho, G. B. Rocha, R. O. Freire, A. M. Simas and J. J. P. Stewart, *J. Chem. Theory Comput.*, 2013, **9**, 3333–3341.

27 M. A. M. Filho, J. D. L. Dutra, G. B. Rocha, R. O. Freire and A. M. Simas, *RSC Adv.*, 2013, **3**, 16747.

28 D. A. Rodrigues, N. B. da Costa and R. O. Freire, *J. Chem. Inf. Model.*, 2011, **51**, 45–51.

29 J. E. Ridley and M. C. Zerner, *Theor. Chim. Acta*, 1976, **42**, 223–236.

30 M. C. Zerner, G. H. Loew, R. F. Kirchner and U. T. Mueller-Westerhofflc, *J. Am.*

Chem. Soc., 1980, **102**, 589–599.

31 F. Neese, *Wiley Interdiscip. Rev. Comput. Mol. Sci.*, 2012, **2**, 73–78.

32 B. R. Judd, *Phys. Rev.*, 1962, **127**, 750–761.

33 G. S. Ofelt, *J. Chem. Phys.*, 1962, **37**, 511–520.

34 N. B. D. Lima, J. D. L. Dutra, S. M. C. Gonçalves, R. O. Freire and A. M. Simas, *Sci. Rep.*, 2016, **6**, 21204.

35 J. D. L. Dutra, T. D. Bispo and R. O. Freire, *J. Comput. Chem.*, 2014, **35**, 772–775.

36 A. J. Freeman and J. P. Desclaux, *J. Magn. Magn. Mater.*, 1979, **12**, 11–21.

37 O. L. Malta, *Chem. Phys. Lett.*, 1982, **87**, 27–29.

38 O. L. Malta, *Chem. Phys. Lett.*, 1982, **88**, 353–356.

39 O. L. Malta, *J. Lumin.*, 1997, **71**, 229–236.

40 F. R. G. e Silva and O. L. Malta, *J. Alloys Compd.*, 1997, **250**, 427–430.

41 O. Kahn, *Molecular Magnetism*, Wiley - VCH, New York, 1st edn., 1993.

42 M. Andruh, E. Bakalbassis, O. Kahn, J. C. Trombe and P. Porcher, *Inorg. Chem.*, 1993, **32**, 1616–1622.